ChemPlusChem

Perspective
doi.org/10.1002/cplu.202400151

Chemistry Europe
European Chemical Societies Publishing

www.chempluschem.org

Design of PtSn Nanocatalysts for Fuel Cell Applications

Monica Distaso*[a, b] and Erika Abella[a]

The challenges in the fuel cell industry lie in the cost, performance, and durability of the electrode components, especially the platinum-based catalysts. Alloying has been identified as an effective strategy to reduce the cost of the catalyst and increase its efficiency and durability. So far, most studies focused on the design of PtM bimetallic nanocatalyst, where M is a transition metal. The resulting PtM materials show higher catalytic activity, but their stability remained challenging. In addition, most of the transition metals M are expensive or low abundant. Tin (Sn) has gained attention as alloying element due to its versatility in manufacturing both anode and cathode electrodes. If used as anode catalyst, it is able to overcome poisoning from CO and related intermediates. As cathode catalyst, it improves the kinetics of the oxygen reduction reaction (ORR). Additionally, Sn is an abundant and cheap element. The current contribution outlines the state of the art on the alloy and shape effect on PtSn activity and stability, demonstrating its high potential to develop cheaper, more efficient and durable catalysts for fuel-cell electrodes. Additionally, *in situ* analytical and spectroscopic studies can shed light on the elementary steps involved in the use of PtSn catalytic systems. Finally, this intriguing material can be used as a parent system for the synthesis of high-entropy-alloys and intermetallics materials.

1. Introduction

In the ever increasing global energy demand, fuel cells stand as a cutting-edge counterpart to conventional batteries, exploiting the power of electrochemistry to transform chemical energy into electricity.[1] With its high conversion efficiency, high energy density and environmental friendliness, the fuel cell technology is a versatile alternative to more traditional power resources in applications spanning from stationary power plants, to vehicles, and compact, portable devices. Despite more than two decades of research and development, the potential of the fuel cell technology remains underexploited, particularly in the transformative sector of Fuel Cell Electric Vehicles (FCEVs).[2,3] The use of fossil fuels in transport and industrial production contributes up to 35% of the global greenhouse gas (GHG) emissions. Additionally, the combustion of fossil fuels releases air pollutants such as nitrogen (NO_x) and sulphur oxides (SO_x), and fine particulate matter, that affect the local and global air quality. Electrification through FCEVs might contribute to mitigate the carbon emissions, and alleviate the environmental impact of the transport sector, providing that the hydrogen used as fuel is entirely produced by renewable energy.[4]

The major challenges in the fuel cell industry lie in the cost, performance, and durability of the electrode components, especially the catalysts, which is indispensable in proton exchange membrane FCEVs.[2,3] It has long been established that platinum-based materials are the best catalysts for both oxidation and reduction reactions. However, being an element of the Precious Metal Group (PMG), Pt is expensive[5] and contributes for around 60% of the cost of the catalyst.[3] The current platinum loadings for FCEVs are typically around 0.53 g/kW for heavy-duty vehicles, and of 0.18 g/kW and 0.13 g/kW for light commercial vehicles and light vehicles, respectively.[3] Efforts are ongoing to reduce these platinum loadings further, with a target of 0.10 g/kW by 2030 set by the US Department of Energy, which appears achievable.[3]

Internal combustion engine vehicles (ICEs) will remain a significant portion of the global mobility well into the 2030 s. ICEs contain comparable lower amount of Pt in the catalytic converters, however, the enforcement of stricter emission regulations worldwide will most probably result in an increase in the demand of PGM catalysts also for ICEs. Therefore, from one side considerable effort is still necessary to achieve cost-competitiveness for FCEV against ICEs. On the other side, the recycling of spent catalysts shall be pushed forward to enable secondary sources of PGMs and avoid risks in the future supply chain.

One strategy to decrease the PGM loading focuses on the manufacturing of the polymer electrolyte fuel cell catalyst through alloying and nanotechnology. Several studies have been conducted to identify the best alloy composition, shape, size, and supporting material for a PGM system with a focus to enhance the catalytic activity. Various bimetallic PtM systems, where M is mostly a transition element, have shown enhanced performance, however, the durability remained a challenge especially for factors such as poisoning and catalyst dissolution. However, it is opinion of the authors that the binary system Platinum-Tin (PtSn) has received comparatively little attention

[a] M. Distaso, E. Abella
Friedrich-Alexander University Erlangen-Nürnberg, Interdisciplinary Center for Functional Particle Systems, Haberstraße 9a, 91058 Erlangen, Germany

[b] M. Distaso
Helmholtz-Institute Erlangen-Nürnberg for Renewable Energy (IET-2), Forschungszentrum Jülich, Cauerstr. 1, 91058 Erlangen, Germany
E-mail: m.distaso@fz-juelich.de

despite its promising performances and intrinsic advantages. Therefore, we focus here on the PtSn binary system, a versatile catalyst that can be used in either the anode or the cathode electrode of fuel cells. In addition, Sn is not a transition metal, it is abundant, and cheap, properties that make it a better alloying component to Pt than Pd, Ag, Ru and other expensive transition metal counterparts that have been on focus up to now. However, Sn belongs to the class of conflict minerals together with Tungsten, Tantalum and Gold (3TG), which might be accounted as an intrinsic disadvantage of this element.[6] This aspect shall be mitigated by the implementation of strict regulations for its international trading to avoid violation of human rights.

The effect of shape and alloy composition will be discussed in more details with supporting analytical techniques that demonstrate its better performance and durability with respect to pure Pt nanoparticles and other PtM nanoparticles. *In situ* spectroscopy studies are fundamental in order to understand better the mechanism beyond the higher catalytic performance and stability of the PtSn systems. Finally, we believe that a better insight in the PtSn system can eventually serve as basis for the development of multicomponent high entropy catalysts, a topic that has recently triggered large interest in the scientific community.[7]

2. Overview of the Fuel Cell Technology

The basic components of a fuel cell are two electrodes, connected externally by a conducting wire, and an electrolyte that separates the two electrodes. Fuel cells are mainly classified based on the electrolyte type since it dictates the chemical reaction that will take place, the fuel, operating temperature, and catalyst required. One of the most studied and developed fuel cell type is the Polymer Electrolyte Membrane Fuel Cell (PEMFC) that has attracted a great deal of attention due to the solid-state nature, the relatively low-temperature operation range (60 °C – 90 °C), and the easy to handle use.[1] A typical PEMFC is operated with hydrogen and oxygen gas as fuels for anode and cathode, respectively. Oxygen is normally introduced as air (Figure 1).[8]

Hydrogen and air are fed into the anode and cathode gas flow channels, respectively. In the anode catalyst layer, hydrogen is oxidized to protons and electrons (Equation 1), which are transported via the membrane and through the external circuit, respectively, to the cathode. There, oxygen is reduced and react with protons to generate energy and water as the only byproduct (Equation 2). The total reaction (Equation 3) is formally the sum of Equation (1) and (2)[8]:

$$H_2 \rightarrow 2\ H^+ + 2\ e^- \quad (1)$$

$$2\ H^+ + \frac{1}{2}\ O_2 + 2\ e^- \rightarrow H_2O \quad (2)$$

$$H_2 + \frac{1}{2}\ O_2 \rightarrow H_2O \quad (3)$$

Despite its apparent simplicity, the implementation of this chemical process is anything but simple. In a first instance, the storage of hydrogen gas is challenging. The current technologies store hydrogen gas physically in its compressed state (37 and 70 MPa), or liquefy it through cryogenic processes at −252.8 °C.[9]

An alternative to compression and condensation is the chemical energy storage, an ensemble of technologies that

Erika Abella holds a bachelor's degree in Chemistry from Polytechnic University of the Philippines and an elite Master's degree in Advanced Materials and Processes from the Friedrich-Alexander-Universität Erlangen-Nürnberg (FAU), Germany. During her master's studies, Erika specialized in Nanomaterials and Biomaterials, and delved into the topic of nanomaterials for fuel cells, and biowaste-derived fuel precursors for her master thesis. She currently hold a position in the pharmaceutical industry, working in the field of Chemistry, Manufacturing and Controls (CMC) Technology and Innovation.

Monica Distaso holds a degree in Inorganic Chemistry and a PhD in Environmental Science from the University of Bari "Aldo Moro", Italy. During her doctoral studies, she developed low environmental impact synthetic methods for the catalytic activation of small molecules, such as carbon dioxide and carbonic acid diesters. In 2009, she joined the Institute of Particle Technology at the Friedrich-Alexander-Universität Erlangen-Nürnberg (FAU), Germany. She is currently team leader at the Forschungszentrum Jülich, Helmholtz Institute Erlangen-Nürnberg for Renewable Energy. She is active in the field of synthesis and characterization of nanomaterials for energy application, with strong focus on understanding reaction mechanisms using multiple and simultaneous in situ analytical and spectroscopic techniques.

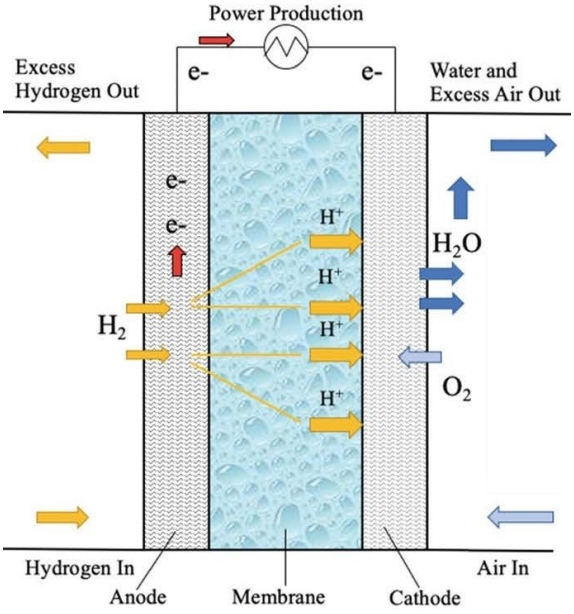

Figure 1. Schematic of the operating principles of PEMFCs. Reproduced from Ref. [8] with permission from the Royal Society of Chemistry.

aims for storing hydrogen in solids, liquids or gases acting as energy carrying compounds. In particular, the Liquid Organic Hydrogen Carrier (LOHC) technology allows high volumetric energy storage density under ambient conditions.[10] LOHC systems consist of pairs of hydrogen-lean, typically aromatic liquids (H0-LOHC), and hydrogen-rich, typically alicyclic liquids (Hx-LOHC).[10] The former store hydrogen in an exothermic catalytic hydrogenation reaction, the latter release hydrogen through an endothermic catalytic dehydrogenation reaction.[11] The LOHC technology is compatible with the current infrastructure for fuels.[12]

Besides the hydrogen storage, an additional crucial aspect of the functioning of fuel cells is related to poisoning. If the hydrogen gas derives from the traditional process of steam reforming of methane or water gas shift reaction it may contain amounts of carbon monoxide (CO) which, even in traces, are able to poison the precious Pt catalyst at the anode of a fuel cell.[13,14]

An alternative to a typical PEMFC is the direct alcohol fuel cell (DAFC), whereby the alcohol is directly fed into the anode with some amount of steam, and oxygen from air is fed into the cathode. This technology is promising due to the possibility to use methanol (DMFC), ethanol (DEFC) or iso-propanol (DIFC) as anode fuel. Long-chain alcohols such as butanol are also promising for their higher energy density and the lower membrane crossover rate compared with ethanol and methanol.[15] However, the butanol obtained from ligno-cellulosic biomass might consist of three isomers, namely the primary alcohol *n*-butanol, the secondary alcohol *iso*-butanol and the tertiary alcohol *ter*-butanol, which show different reactivity in direct fuel cells.[15,16] Ethanol, instead, is highly abundant and can be easily obtained on large scale through sugar fermentation processes.

The reaction cascade of the alcohol oxidation reduction (AOR) specific to methanol as fuel is reported in Figure 2. During the AOR, methanol is not directly oxidized to carbon dioxide due to a partial oxidation reaction that produces formaldehyde (HCHO), formic acid (HCOOH), or adsorbed carbon monoxide (CO_{ads}).[17]

With DEFC technology, the challenge lies in the only partial oxidation of the alcohol leading to the formation of intermediates such as CO, CH_3COOH, and CH_3CHO which are poisonous to Pt and must be avoided.[14]

The adsorption of ethanol onto the surface of Pt is a complex phenomenon that depends on various factors such as the facets of platinum, the voltage applied and the relative coverage of the surface. Therefore, under the dynamic conditions of a Direct Ethanol Fuel Cell (DEFC) various configurations and paths for the dissociative adsorption of ethanol are possible, as summarized in Figure 3.[18]

On the other hand, *iso*-propanol as fuel offers several advantages with respect to methanol. In a first instance, the use of *iso*-propanol does not lead to the formation of carbon dioxide (CO_2), making the DIFC a good choice for the transition to greener DAFC technology. The lack of CO_2 formation also indicates that the occurrence of CO-related intermediates is limited, in contrast to the methanol reaction cascade (Figure 2), hence lowering the chance of catalyst poisoning.

Iso-propanol converts directly into acetone (Equation 4), whereas the conversion of iso-propanol to CO_2, requires another step of chemical conversion (Equation 5). In addition,

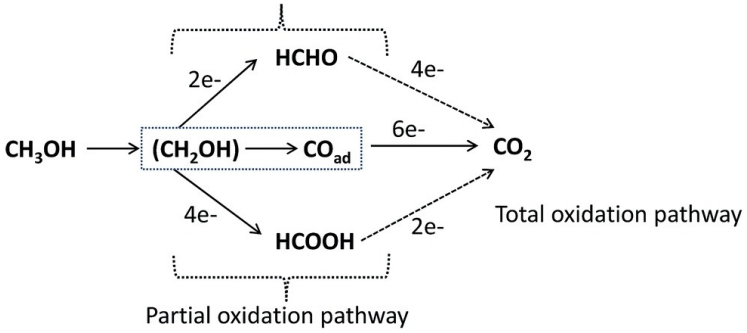

Figure 2. Schematic of the Methanol Oxidation Reaction. Reproduced from Ref. [17] with permission from the Royal Society of Chemistry.

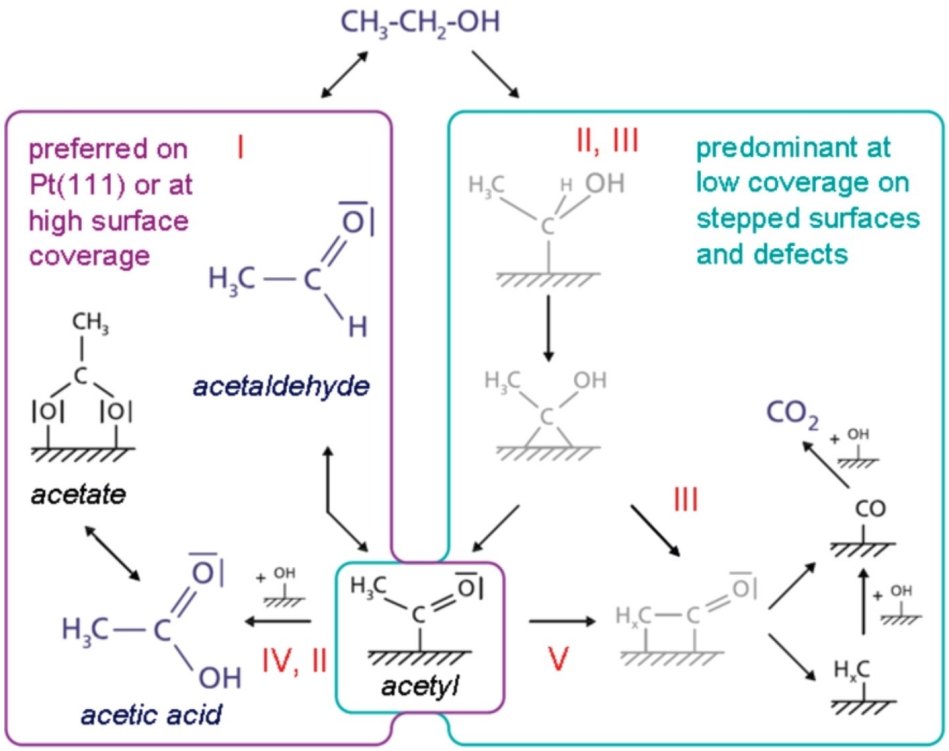

Figure 3. Summary of the ethanol oxidation reaction (EOR) mechanism on Pt. Path on the left is preferred onto Pt(111) and at high surface coverages and the path on the right side is dominant at low coverages on stepped surfaces and defects. Adsorbates pictured in black were found experimentally and molecules in blue are present in solution. Reprinted with permission from Melke, J.; Schoekel, A.; Dixon, D.; Cremers, C.; Ramaker D. E.; Roth, C. Ethanol Oxidation on Carbon-Supported Pt, PtRu, and PtSn Catalysts Studied by *Operando* X-ray Absorption Spectroscopy. *J. Phys. Chem. C* **2010**, *114*, 5914–5925. Copyright 2010 American Chemical Society.

the conversion of isopropanol to acetone occurs at lower potential with respect to the total oxidation to carbon dioxide. Altogether, the isopropanol to acetone transformation is more favorable compared to isopropanol to carbon dioxide total oxidation.

$$CH_3CH(OH)CH_3 \rightarrow CH_3C(O)CH_3 + 2\ H^+ + 2\ e^- \quad (4)$$

$$CH_3C(O)CH_3 + 6\ OH^- \rightarrow 3\ CO_2 + 11\ H_2O + 16\ e^- \quad (5)$$

An interesting concept combines the DIFC with the LOHC technology (Figure 4).[11] Shortly, a hydrogen rich liquid organic compound such as perhydro dibenzyl toluene (H18-DBT) undergoes a sequence of transfer hydrogenation reactions of acetone to iso-propanol. The formed iso-propanol is used as organic fuel in a subsequent PEM fuel cell, whereby the acetone produced is recycled and undergoes another cycle of transfer hydrogenation and electrification (Figure 4).[11] The transfer hydrogenation reaction (THR) is thermo-neutral, as the heat of the endothermal H18-DBT dehydrogenation equals approximately the heat of the exothermal acetone hydrogenation per mole of hydrogen transferred.[11] On the other side, the combination of LOHC and the DIFC does not produce any CO_2 emissions, due to the stability of the C–C bond in the secondary alcohol.[11]

Thus, considering the safety and easy of handling, DAFC seems to be a promising substitute to PEMFC. In a typical PEMFC, hydrogen oxidation reaction (HOR, Equation 1) and oxygen reduction reaction (ORR, Equation 2) are the two main chemical transformation in the anode and cathode, respectively. In DAFC, the anodic reaction as HOR changes to alcohol oxidation reaction (AOR), whereas the cathode reaction remains as ORR. Being HOR the dissociation of hydrogen to proton and electron, it is a relatively fast process, which requires a relatively lower catalyst loading on the anode with respect to the ORR content in the cathode. On the contrary, ORR is known to be the limiting step in a PEMFC reaction, which has a five times slower rate than HOR and requires an overpotential. Consequently, it has been estimated that 80–90% of the total Pt in the stack is in the cathode.[1,19] The limiting ORR is applicable for both PEMFC and DAFC. As discussed,[3,5] most of the cost in fuel cell manufacturing is due to the use of Pt catalyst, therefore it is of utmost importance to utilize and conserve every amount of it in designing a fuel cell.

The state-of-the-art catalyst used for DAFCs is platinum-ruthenium or PtRu, mainly due to its superior anti-poisoning property against CO.[20,21] It has also been the catalyst of interest for DIFCs due to its ability to activate isopropanol at low overpotential.[22,23] In alkaline electrolytes, other noble metals besides Pt, such as Pd, Au and Rh, are active catalyst for the oxidation of iso-propanol to acetone.[24]

Ruthenium is one of the rare-element metals and the abundancy is 0.0004 parts per million of the earth's crust.[25]

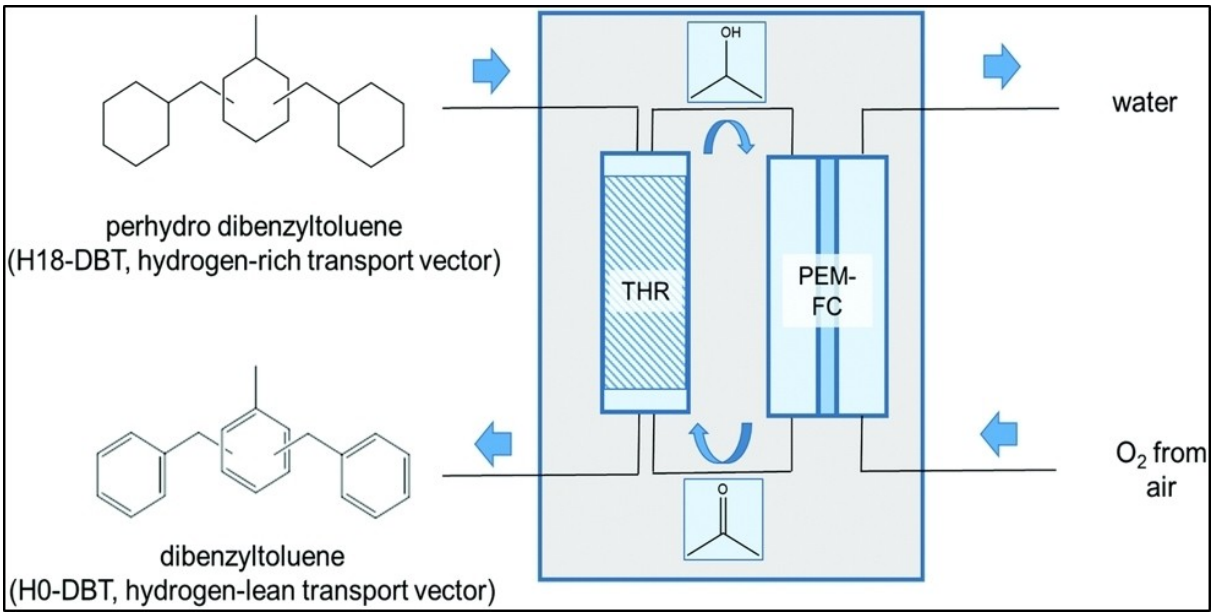

Figure 4. Schematic of the LOHC-DIFC system. Reproduced from Ref. [11] with permission from the Royal Society of Chemistry.

Additionally, Ru is a critical raw material together with the other elements of the Pt-group, indicating that besides its technological relevance there exist a substantial risk of supply.[26] Therefore, it can be assumed that, like platinum, a supply chain and the cost-related problem might also be a hindrance to the usage of ruthenium in the future.

2.1. Structural Parameters in Multicomponent Nanocrystals

Since the discovery that gold clusters, differently for their bulk counterpart, are able to oxidize CO at relatively low temperature,[27] there has been a remarkable interest for exploring the potential of metal nanoparticles as effective catalysts in a number of different chemical reactions. The fascinating properties of nanocatalysts are remarkably enhanced when a second element is added, as superior materials are achieved due to synergistic effects between the elements. The enhancement of the catalytic properties both in monometallic, binary or multi-metallic systems is mainly due to the surface effect that can be manipulated in terms of size, shape, composition and order (Scheme 1). The size and shape effect on nanocatalyst performance are interlinked through the exposure of facets with different stability and reactivity. The development of certain facets with respect to others can be exerted through the selection of suitable ligands, reducing agents, metal precursors and growth conditions.[28] In Scheme 1, the variation in composition is schematically depicted as increase in the shell thickness for a core-shell system, retaining the particle size and shape. Finally, under the term "order" in Scheme 1, we understand the structure and crystal phase of the nanocrystals that highly affect the catalyst performance. The composition and order are highly interconnected; however the composition alone is not sufficient to rationalize the nanocrystal properties. For example, it has been demonstrated that bimetallic PtM nanocrystals with the same composition bear completely different catalytic properties depending on the degree of order at atomic scale. Accordingly, FePt intermetallic nanocrystals showed high chemical stability and electrocatalytic activity toward ORR and hydrogen evolution reaction when their crystal phase was changed from the atomically disordered phase to the ordered phase.[29]

Therefore, the structural parameters reported in Scheme 1 are strongly interlinked with each other, and seldom can they be addressed independently. Nevertheless, it is of paramount importance to control them tightly, as they define the properties of the materials at hands. Accordingly, various synthetic protocols have been developed to enhance the catalytic properties of nanocrystals via properties control. Table 1 summarizes the various studies on the synthesis of PtSn where variation of the size, shape, composition and order have been correlated with the catalyst performance. In the current contribution, we will shed light on the influence of structural parameters on the electrocatalytic properties of PtSn nanocrystals using the available scientific literature. In section 3, we will describe the state of the art on the implementation of *in situ* analytical and spectroscopic techniques to shed light on the elementary steps and on the mechanism of various electrochemical reactions, and for comparison, of some thermal processes.

2.2. Motivation Towards PtSn Nanocatalysts

In nanocatalyst research, most bimetallic nanocatalysts are in the form of PtM where M is any transition element. However, the stability and durability of the PtM catalyst is still in question as it is desirable to not only increase the activity of PtM catalyst

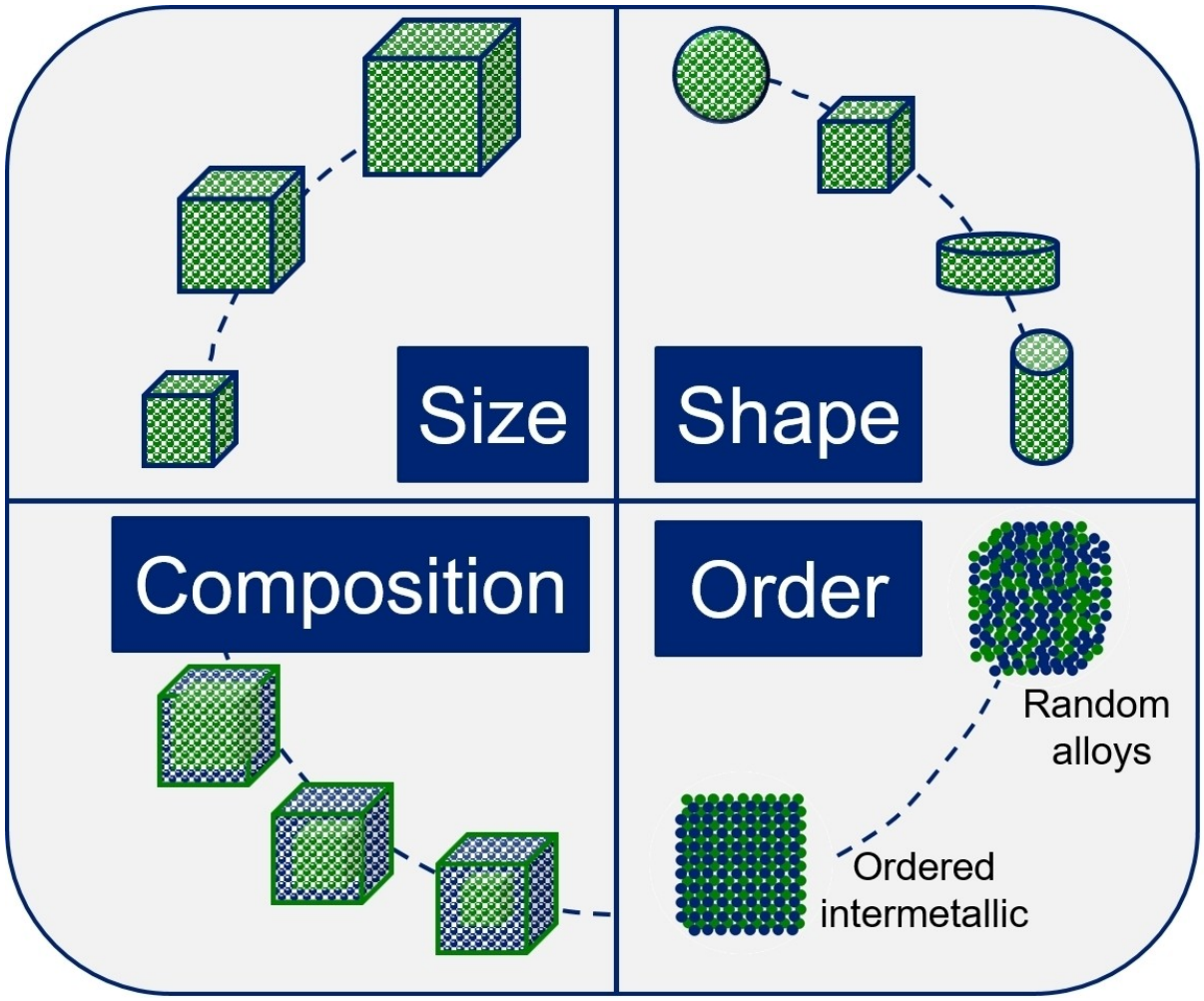

Scheme 1. Structural parameters determining the properties of bimetallic nanocrystals.

but also manage the stability of the catalyst over time so that process specific mitigation steps can be minimized. Hence, though it is well known that PtM is more active than pure Pt counterpart, broader PtM combinations, where M may be or may not be a transition element, are further explored to achieve higher catalyst stability. As an example, PtRu, PtPd and PtSn on carbon black (Vulcan XC-72) were investigated as catalyst for the electrochemical oxidation of methanol. The results of the study show that the PtSn/C system has better catalytic activity than the other synthesized catalysts except for PtRu/C, however, the Pt/C system was more stable than the PtSn/C (Table 1, Entry 1).[30]

It is of critical importance to rationalize this kind of results in a large framework to account for both the reactivity between different metal systems, and stability with respect to the monometallic Pt counterpart. A good visual overview that correlates activity and stability was provided by Guo et al.[31] The authors reported a computational study of various bimetallic PtMs, where M was Co, Ni, Cu, Rh, Pd, Ag, Ir, Au, or Sn (Table 1, Entry 2). In terms of computational parameters, the authors considered the segregation energy before and after the electrochemical cycling.[41] The segregation energy of a clean surface, $E_{seg,}$ and upon adsorption of oxygen-containing species (OCS) during ORR, $E_{seg\text{-}OCS}$, respectively are reported in Equation 6 and 7, respectively:

$$E_{seg} = E_{M-subsurface}(PtM) - E_{M-surface}(PtM) \quad (6)$$

$$E_{seg-OCS} = E_{M-subsurface}(PtM - OCS) - E_{M-surface}(PtM - OCS) \quad (7)$$

where $E_{M\text{-}subsurface}(PtM)$ and $E_{M\text{-}surface}(PtM)$ are the energies of the loaded M in the subsurface and on the surface, respectively, on the clean PtM (Equation 6). Similarly, $E_{M\text{-}subsurface}(PtM\text{-}OCS)$ and $E_{M\text{-}surface}(PtM\text{-}OCS)$ are the energies of PtM subsurfaces and surfaces upon adsorption of the oxygen containing species (Equation 7). Positive values of the E_{seg} and $E_{seg\text{-}OCS}$ indicate that M is thermodynamically stable on both the surfaces of clean PtM for the as-prepared catalyst and OCS adsorbed PtM during the ORR. On the contrary, negative values of E_{seg} and $E_{seg\text{-}OCS}$ imply that M is preferentially located in the subsurface. As long as E_{seg} and $E_{seg\text{-}OCS}$ have the same sign (either positive or negative), M will stay in the same position (i.e. surface or subsurface, i.e. shell, or core) and PtM will be thermodynamically stable before and under ORR operation. On the other

Table 1. Summary of the studies on the synthesis and electrochemical characterization of various PtSn systems.

Entry	Catalysts	Reaction	Conclusions	Ref.
1	PtRu/C, PtPd/C, PtSn/C	MeOH Ox	Reactivity: PtSn/C > PtRu/C, Stability: Pt/C > PtRu/C	[30]
2	PtSn vs PtM (M=Pd, Ag, Au, Ni, Ir, Co, Cu, Rh)	ORR	Stability PtSn > PtM; PtPd and PtAg borderline	[31]
3	PtSn@Pt, PtSn IMs vs Pt, PtRu, and PtSn alloys	H_2 Ox	CO tolerance: PtSn@Pt > PtSn IMc > Pt, PtRu, PtSn	[32]
4	PtSn	Ox of H_2, CO, H_2/CO	CO tolerance of Sn/SnO_2 (bifunctional mechanism)	[33]
5	Pt *vs* PtSn	DAFC (butanol)	Bifunctional mechanism, reactivity butanol isomers	[15]
6	Pt/Ru, Pt/Mo and Pt/Sn alloys	DFT study on CO Ox	In Pt_3Sn(111) CO binds to Pt and OH on Sn	[34]
7	PtSn vs Pt	CO Ox	Ligand mechanism	[35]
8	Synthesis of PtSn alloys and Pt_3Sn IMs	hot-injection	Tuneable shapes, IMc above 250 °C	[36]
9	PtSn NPs with various Sn amount and constant size (3–5 nm)	DAFC (ethanol)	Increase of the cell potential by increasing the Sn content→higher performance of the PtSn system	[37]
10	Narrow distributed PtSn NPs	EtOH Ox	Presence and contribution of SnO_2 in PtSn	[38]
11	PtSn *vs* Pt nanocubes Pt-rich core, with a Sn-rich subsurface layer, and a Pt-skin surface structure	EtOH Ox	Activity: Cubic PtSn > 3 unshaped PtSn NPs; Cubic PtSn > Pt nanocubes; PtSn excellent durability	[39]
12	PtSn NPs *vs* PtSn NWs	ORR	ADT of 10,000 cycles; PtSn NWs maintained the diameter and showed minimal length degradation	[31]
13	IMs Pt_3Sn/C NFs with different aspect ratio, *vs* Pt_3Sn NP/C and Pt/C	AOR (EtOH)	1 D structures show less degradation; Improved mass/charge transport; higher AR, higher catalyst performance; High CO tolerance	[14]
14	2D-NPs of sub-1-nm PtSn hexagonal-ultrathin sheet vs commercial Pt black and Pt/C catalysts	AOR (MeOH and EtOH)	2D sheets exhibited better activity and durability; the exposure of Pt(111) facets is beneficial	[40]

Ox = oxidation; ORR = Oxygen Reduction Reaction; IMs = intermetallics; NPs = nanoparticles; NWs = nanowires; ADT = Accelerated Durability Test; NFs = nanofibers; AOR = Alcohol Oxidation Reaction; AR = Aspect Ratio.

hand, different signs of E_{seg} and $E_{seg\text{-}OCS}$ suggest the change in position of M during the electrochemical cycling and hence indicate poor stability of the PtM system. E_{seg} and $E_{seg\text{-}OCS}$ were plotted in x-axis and y-axis, respectively (Figure 5).

PtSn has both positive E_{seg} and $E_{seg\text{-}OCS}$ compared to other PtM combinations, which have a dissimilar sign of E_{seg} and $E_{seg\text{-}OCS}$. This suggests that PtSn will be in place and is thermodynamically stable before and during ORR. The PtSn stability is attributed to the synergistic effects of the larger Sn radius and its higher oxophilicity compared to Pt. Namely, the larger radius of Sn makes it thermodynamically stable to be on the shell of a PtSn core-shell particle. The Sn has stronger bonding with oxygen-containing species that results in the weaker adsorption of ORR intermediates on the Pt surface thus improving the ORR performance.

In the following sections, studies carried out to understand the impact of the alloy and shape effect on PtSn will be reviewed in depth. Emphasis will be on performance indicators obtained from structural characterization via X-ray diffraction (XRD), transmission electron microscopy (TEM), electrochemical measurements such as mass activity (MA), electrochemical surface activity (ECSA), cell current density, resistance, and mass transport after several cycles. Accelerated durability tests (ADT) will be discussed with the help of exemplary research to finally give a general view of the status and future developments of this intriguing material system.

2.3. The Alloy Effect

Aside from lowering the cost, bimetallic nanoparticles PtM where M is a non-transition metal show enhanced catalytic activity and selectivity with respect to the monometallic counterpart. Such enhanced properties are attributed not only to the composition but also to the specific structural arrangement at nanoscale. The arrangement can be random or disordered, leading to a random-alloy system. Alternatively, the metals can be arranged in a crystalline and ordered manner leading to intermetallic systems.[36]

Bimetallic nanoparticles outperform the monometallic counterpart mainly via geometric (ensemble) effects and electronic (ligand) effects. Geometric effects come upon the preferential location of the metal ions in a structure, which eventually changes the interaction of the adsorbates onto the surface of the bimetallic catalyst as compared to the monometallic counterpart. On the other side, electronic effects result from the change of the valence electronic structure of the surface due to the change of the local environment. The two effects are frequently interlinked and difficult to be identified

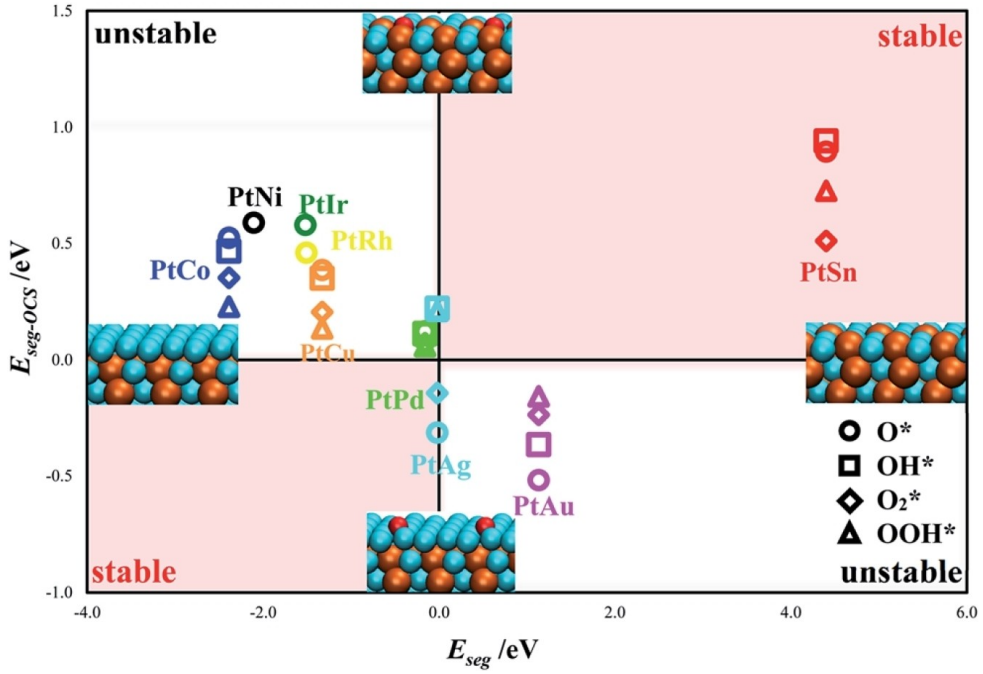

Figure 5. Segregation energies before and during ORR of various bimetallic PtM catalyst (M=Co, Ni, Cu, Rh, Pd, Ag, Ir, Au, and Sn). E_{seg} is the segregation energy of a clean surface (Equation 6), whereas $E_{seg\text{-}OCS}$ is the segregation energy upon adsorption of oxygen-containing species (OCS) during ORR (Equation 7). Reproduced from Ref. [31] with permission from the Royal Society of Chemistry.

separately.[42,43] Pt and Sn form solid solutions of any stoichiometry, either in faced centred cubic (fcc) phase for Sn < 25 at.% or in hexagonal closed packed (hcp) phase for higher Sn contents. The most widely studied systems are the hcp PtSn and the fcc Pt_3Sn intermetallic phases. Liu et al. reported that PtSn@Pt core–shell and the PtSn intermetallic electrocatalysts have substantially higher tolerance to CO-poisoning compared to Pt, PtRu alloy, and PtSn alloy catalysts (Table 1, Entry 3). The higher CO-tolerance of the PtSn@Pt system was attributed to the electronic effect of the PtSn core on the Pt shell, while the high CO-tolerance of the intermetallic was assigned to the bifunctional mechanism.[32] Such bifunctional mechanism generally refers to the preferential oxidation of CO adsorbed onto Pt in a PtM bimetallic surface via an oxygen-containing species adsorbed on the nearby species M. However, this mechanism does not consider that the binding energy of CO on Pt might be changed by the presence of M through the electronic effect. Additionally, the oxygen containing species (usually described as a hydroxyl species, OH) and CO might compete for the adsorption sites on the second metal, M. The literature is univocal in the observation that in comparison with pure Pt, the Sn modified Pt surface promotes the formation of OH species adsorbed onto the catalyst surface at a lower onset potential. One of the first studies devoted to shed light on the mechanism of Sn/SnO_2 promotion dates to 2005 (Table 1, Entry 4).[33] The authors studied in detail the adsorption of CO onto carbon-supported PtSn nanocatalysts for the anodic oxidation of hydrogen, carbon monoxide, and H_2/CO mixtures and identified the following elementary steps (Equation 8–12):

$$Pt^* + CO_{diss.} = Pt{-}CO_{ad} \quad (8)$$

$$Sn^* + H_2O = Sn{-}OH_{ad} + H^+ + e^- \quad (9)$$

$$SnO_2{}^* + H_2O = SnO_2{-}OH_{ad} + H^+ + e^- \quad (10)$$

$$Pt{-}CO_{ad} + Sn{-}OH_{ad} = CO_2 + H^+ + e^- \quad (11)$$

$$Pt{-}CO_{ad} + SnO_2{-}OH_{ad} = CO_2 + H^+ + e^- \quad (12)$$

Therefore, a continuous oxidative removal of adsorbed CO occurs and takes place already at low potential (below 0.1 V). Due to the absence of back-bonding in potential dependent FTIR spectra, the authors suggested that the promotion effect of Sn/SnO_2 is due to a bifunctional mechanism rather than to a ligand effect.[33,44] More recently, the elementary steps in Equation 8–12 have been confirmed also for the direct butanol fuel cell using *in situ* FTIR spectroscopy and cyclic voltammetry, whereby the authors carry out a comparison between Pt and PtSn electrocatalysts and draw conclusions about the different reactivity of the butanol isomers (Table 1, Entry 5).[15]

Shubina and Koper carried out a periodic density-functional theory study of the adsorption of carbon monoxide (CO) and hydroxyl (OH) on Pt/Ru, Pt/Mo and Pt/Sn alloys (Table 1, Entry 6). The calculations show that for the system $Pt_3Sn(111)$, CO binds only to Pt and not to Sn, whereas OH has an energetic preference for the Sn sites.[34] Using an *ad hoc* synthesized catalyst consisting of a thin layer of Sn onto the surface of Pt, Huang et al. studied the electro-oxidation of CO to specifically understand the bifunctional mechanism.[35] They concluded that

the CO oxidation occurred at lower potentials, because the Pt–CO bond is weakened via a combination of ligand effects from strong Pt–Sn intermetallic bonds and the intermolecular repulsion between the co-adsorbed Pt–CO and Sn–OH.[35]

In the study by Wang et al., a hot-injection method with varying PtSn ratios demonstrated a controllable synthesis route to produce different morphology and structure of PtSn alloy (Table 1, Entry 8).[36] The 90:10 PtSn displayed a flower-like shape and based on the XRD characterization it resulted to be a random-alloy (Figure 6a). A ratio of 80:20 PtSn exhibited instead a mixture of different morphologies such as cubic, tetrahedral, cross-, star-, or heart-like and is similar to Pt_3Sn intermetallic structure, as confirmed by the additional small Bragg reflections (Figure 6b). From this study, it is also worth to emphasize that temperature also plays a crucial role in the formation of intermetallics. Synthesis via hot-injection approach at reaction temperatures below 250 °C do not lead to the formation of intermetallic materials. In fact, Wu et al. demonstrated that PtSn NCs are formed through an initial reduction of Pt(II) to form Pt NCs, followed by the fast diffusion of Sn into the Pt lattice. However, their *in situ* synchrotron X-ray scattering study showed that the reordering of Pt and Sn atoms into intermetallic PtSn structure occurred within 300 s at around 280 °C.[45]

In a study by Colmati et al.,[37] the formation of distinct PtSn bimetallic systems with systematic variation of the Sn amount were investigated with respect to the electronic and structural property (Table 1, Entry 9). In this study, the authors were able to keep the average particle size constant to values between 3 and 5 nm, independent of the Sn content. Figure 7a shows the microstructural characterization of various PtSn intermetallic particles and the corresponding cell potential measured at a constant current of 0.02 A cm^{-2} (Figure 7b). By increasing the Sn content, the cell potential increases too, indicating an enhanced DEFC performance. With Pt_1Sn_3/C intermetallic system, the cell potential decreases due to the lack of active Pt sites. The study sheds light on the understanding of other effects besides the increase in Sn content by comparing material with same Sn ratio but different properties. For example, two bimetallic catalysts exhibit different cell potential even if they have the same Pt and Sn ratio (Figure 7b). Namely, the commercially available Pt_3Sn_1/C (ETEK) has a higher cell potential of almost 100 mV compared to the as-prepared Pt_3Sn_1/C. This observation was attributed to the fact that the formation of SnO_2 particles in the vicinity of the PtSn solid solution enhances the DEFC performance.[46,47] This observation is confirmed by the XRD results as shown in Figure 7a. The reflection at around 50 2θ°are due to the tetragonal SnO_2 phase and an increasing intensity is observed in the order Pt_3Sn_1/C < Pt_3Sn_1/C (ETEK) < Pt_1Sn_1/C. The presence of the SnO_2 phase enhances the electrochemical performance by providing oxidation sites for CO, which thus resulted in lower poisoning effect to Pt and longer durability of the catalyst. Additionally the authors studied the effect of annealing temperature on the catalytic performance of the PtSn systems. In Figure 7c, the results of the annealing obtained for Pt_3Sn/C are reported and demonstrate that by increasing the annealing temperature the cell potential increases up to a temperature of 200 °C, and then drops to values slightly above those observed for the non-annealed sample. To rationalize these results, the authors analyzed the change in the lattice parameter for the thermal annealed samples and found that it increased from a = 0.3959 nm for the as-prepared Pt_3Sn_1/C to a = 0.4000 nm for the thermally treated samples, a value which is closer to the Pt_3Sn intermetallic phase. This suggests that the enhancement of the catalytic activity was due to an increase in the atomic scale order of the nanocrystals (Scheme 1 and Figure 7).

Further increase of the annealing temperature, lead to the formation of additional phases, and the narrowing of reflections, indicating an increase in the crystallite size. The effect of SnO_2 was previously observed by Godoi et al. for narrowly distributed PtSn nanocrystals.[38]

Taken together, these data demonstrate the complex interplay between size, composition and atomic scale order on the

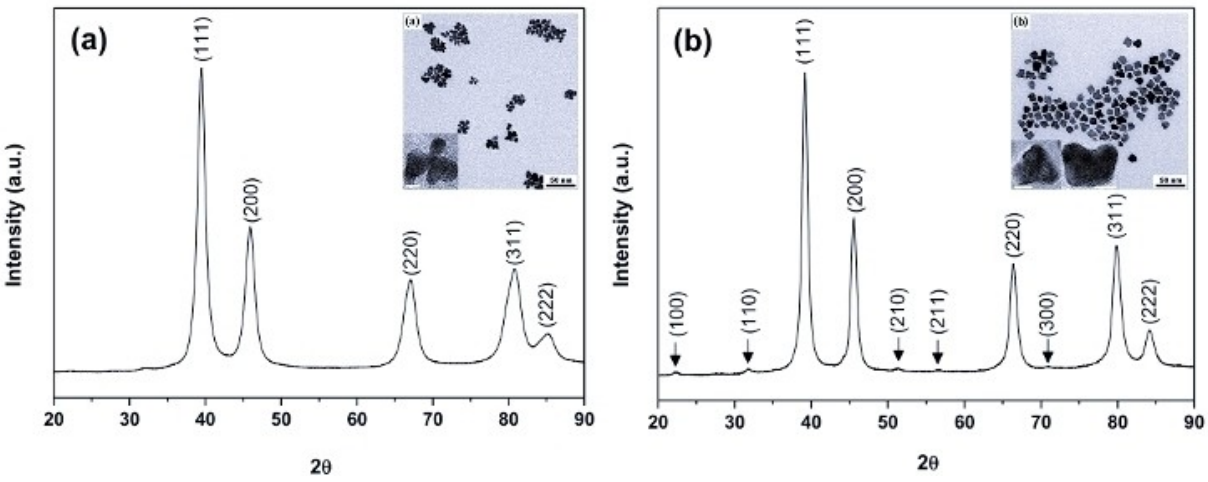

Figure 6. XRD pattern with TEM image inset of Pt:Sn at different molar ratios (a) 90:10 and (b) 80:20 Reprinted with permission from Wang, X.; Altmann, L.; Stoever, J.; Zielasek, V.; Bäumer, M.; Al-Shamery, K.; Borchert, H.; Parisi, J.; Kolny-Olesiak, J. Pt/Sn Intermetallic, Core/Shell and Alloy Nanoparticles: Colloidal Synthesis and Structural Control, *Chemistry of Materials*, **2013**, *25*, 1400–1407. Copyright 2013 American Chemical Society.

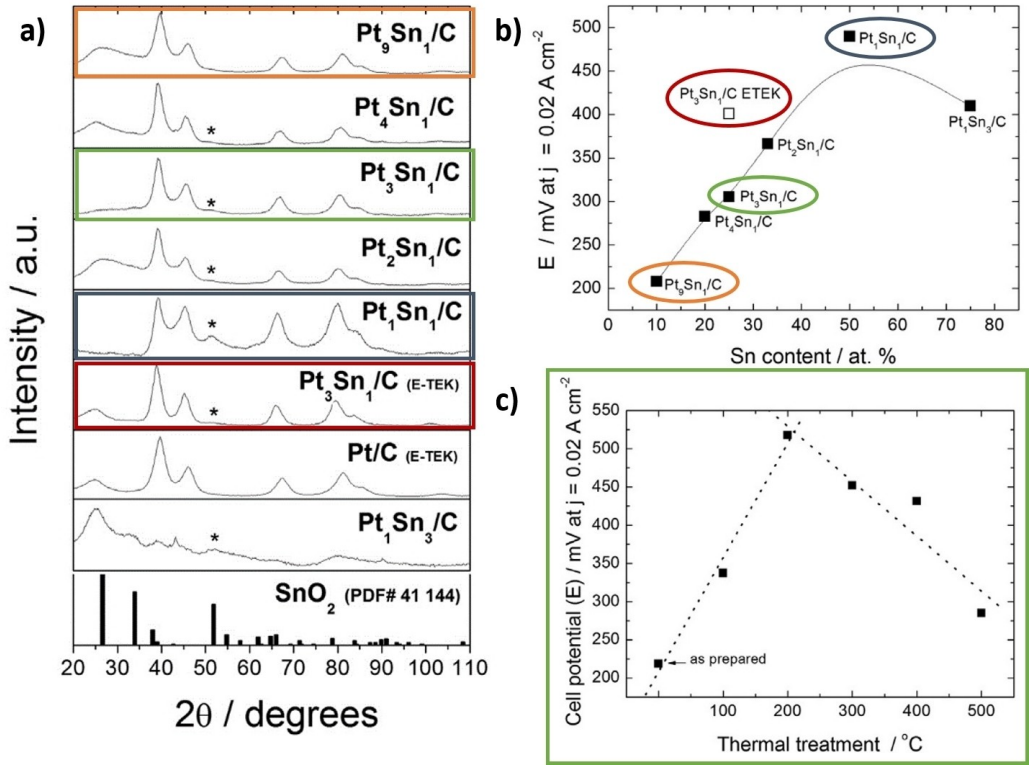

Figure 7. a) XRD patterns of different PtSn intermetallic systems; b) cell potential as a function of Sn content (at %); c) effect of the thermal treatment on Pt_3Sn/C catalysts in the cell performace of a DEFC. These figures were published in *International Journal of Hydrogen Energy*, 44, F. Colmati, M. Magalhães, R. Sousa, E. Ciapina and E. Gonzalez, Direct Ethanol Fuel Cells: The influence of structural and electronic effects on Pt–Sn/C electrocatalysts, 28812–28820, Copyright Elsevier (2019).[37]

performance of DEFC. The higher order achieved through a higher incorporation of Sn in the crystal lattice of Pt leads to a lower amount of unoccupied 5 d states, an electronic effect that together with the presence of an adjacent SnO_2 phase is considered by the authors as the fundamental factor responsible for the observed catalytic performance. However, the nature of the SnO_2-PtSn topology remained undisclosed in this study.[37]

In conclusion, various studies are trying to optimize the formation of intermetallic systems rather than random-alloys due to their promising tailorable and unique properties.

2.4. The Shape Effect

Nanotechnology has demonstrated an unprecedented ability to control the properties of matter at nanoscale. Through the precise manipulation of experimental conditions, selection of precursors and additives during the synthesis, the shape of nanocrystals can be driven to adjust the nature of the exposed facets and the abundance of defects like steps, edges, and kinks, which serve as hotspots for catalysis.[28] Through nanotechnology, scientists can fine-tune the physical and chemical properties of catalysts, unlocking new pathways to enhance reaction mechanisms and drive forward the boundaries of catalytic research.[42]

The effect of shape on the catalytic activity of PtSn nanocatalysts was also investigated (Scheme 1) and is summarized in Table 1 (Entry 11–14).

For example, Rizo et al. studied the oxidation of ethanol using PtSn nanocubes as electrocatalysts (Table 1, Entry 11). They observed that the catalytic activity of cubic PtSn nanoparticles was about three times higher than for the unshaped PtSn nanoparticles and six times higher than that of Pt nanocubes. Moreover, the PtSn electrocatalyst reported greater durability with negligible loss of specific surface area after 5,000 cycles. Such excellent performance was attributed to the peculiar architecture of the electrocatalyst, consisting of a Pt-rich core, a Sn-rich subsurface layer, and a Pt-skin surface structure.[39]

In another important study, the performance of nanoparticles (PtSn1 NP) and nanowires (PtSn9 NW) was compared after an accelerated durability test (ADT) of 10,000 cycles (Table 1, Entry 12). The change in morphology and electrochemical results before and during ORR were compared. The TEM images in Figure 8 a-d show that PtSn1 NP aggregate and coarsened, while the PtSn9 NWs maintained their diameter and showed minimal degradation in length. To rationalize this result, the authors measure the mass activity (MA), a parameter that quantifies how much current can be obtained over a certain Pt-loading. It was found that the MA increases as the aspect ratio increases, thus PtSn9 NW has a higher MA of 119 mA/mg_{Pt} compared to PtSn1 NP with an MA of 95 mA/mg_{Pt}.

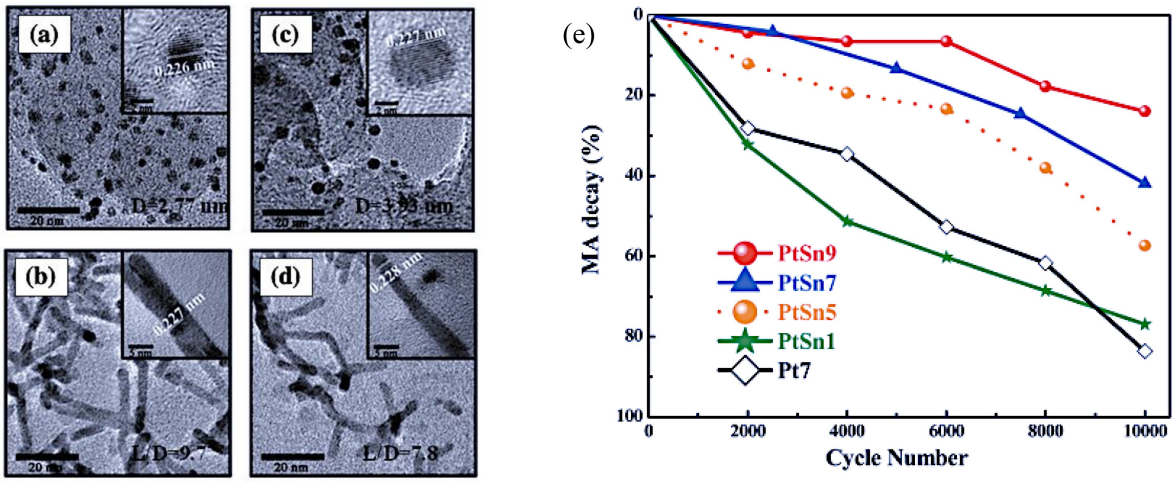

Figure 8. PtSn1 NP a) and c), PtSn9 NW (b) and (d) before and after ADT, respectively. Inset is the lattice parameter of Pt (0.227 nm); e) mass activity (MA) decay of various PtSn morphology. PtSn1 is the nanoparticle, PtSn5, PtSn7, and PtSn9 are the nanowires in increasing aspect ratio (L/D). Reproduced from Ref. [31] with permission from the Royal Society of Chemistry.

The increasing trend in MA with respect to aspect ratio can therefore be attributed to the structure sensitivity of Pt-based nanocatalyst. It is known that the activity of the facets increases in the following order Pt (100) ≪ Pt(111) ≪ Pt(110). The XRD results further revealed that PtSn9 NW has a higher Pt(111) area ratio compared to PtSn1 NP. The decay of MA with respect to ADT of 10,000 cycles was also investigated. As shown in Figure 8 e, the MA decay after 10,000 cycles is insignificant for PtSn9 NW compared to PtSn1 NP. This can be explained by the asymmetric structure of the NWs that makes them less vulnerable to dissolution, aggregation, and Ostwald ripening.[31]

A similar study from Zhu et al., who investigated the intermetallic Pt_3Sn/C nanofibers (NF) with different aspect ratios, showed as well that higher aspect ratio enhances the performance of the catalyst (Table 1, Entry 13). Electrochemical Impedance Spectroscopy (EIS) of Pt_3Sn NF/C, Pt_3Sn NP/C, and Pt/C is shown in Figure 9. It can be seen that Pt_3Sn NF/C have better conductivity and smaller charge transfer resistance than Pt_3Sn NPs/C and Pt/C. The enhanced property was attributed to the ability of 1D nanostructure to provide a better structural foundation (lesser degradation and aggregation) and mass/charge transport. Besides, varied lengths of NF can improve the interaction as well with the carbon support.[14]

The aforementioned research also investigated the anti-poisoning ability of NFs from intermediates, especially carbon monoxide (CO) during Alcohol Oxidation Reaction (AOR). To mimic a worst-case environment, CO was directly purged into the reaction at 200 s and let the reaction run until 5000 s to monitor the change in the current before and after the CO-purging. Chronoamperometry (CA) results in Figure 10 showed that after CO injection, the current density of Pt/C drastically dropped to 0% while Pt_3Sn NF/C and Pt_3Sn NP/C was able to retain 32% and 13% of the initial current density after 5000 s, respectively. Hence, the result strongly suggests not only the

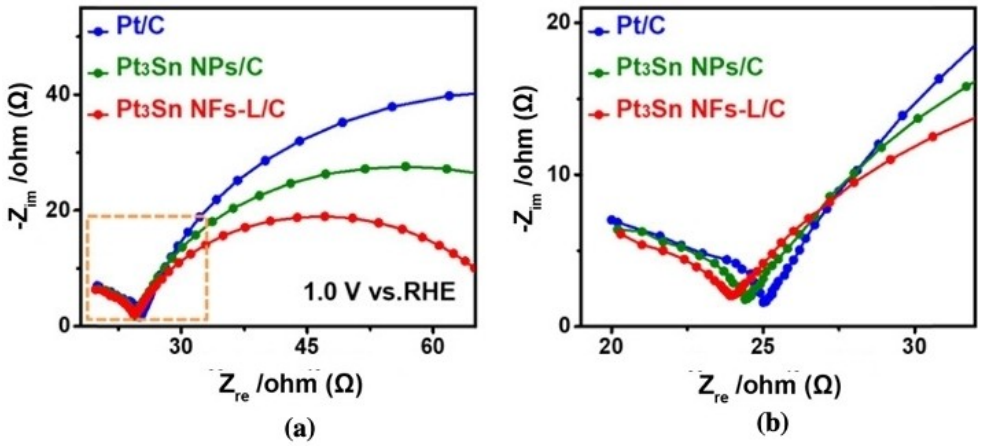

Figure 9. (a) Nyquist Plot of Pt_3Sn NF, Pt_3Sn NP and Pt/C and (b) zoomed-in region for resistance measurement. Reprinted with permission from Zhu, Y.; Bu, L.; Shao, Q.; Huang, X. Structurally Ordered Pt_3Sn Nanofibers with Highlighted Antipoisoning Property as Efficient Ethanol Oxidation Electrocatalysts, *ACS Catalysis*, **2020**, *10*, 3455–3461. Copyright 2020 American Chemical Society.

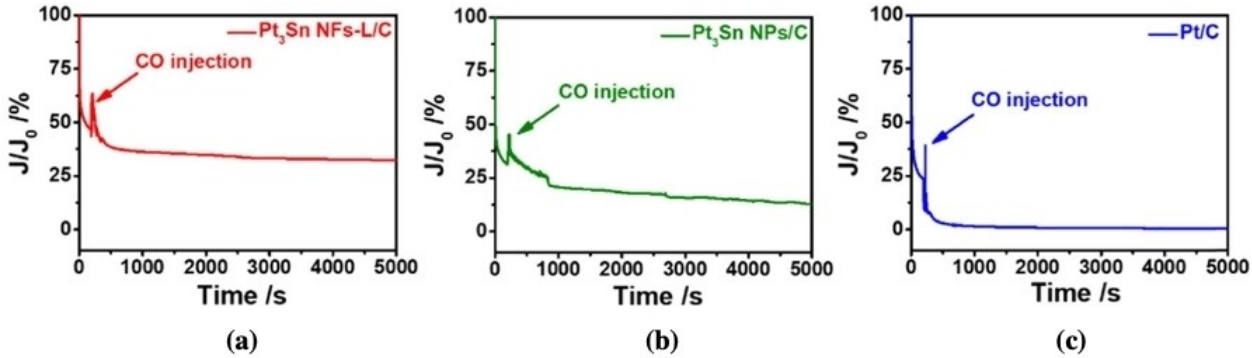

Figure 10. CA result at 1.0 V after CO-purging at 200s and reaction time of 5000s (a) Pt_3Sn NFs–L/C, (b) Pt_3Sn NPs/C, and (c) Pt/C in 0.1 M $HClO_4$ + 0.5 M CH_3CH_2OH solution.[14] Reprinted with permission from Zhu, Y.; Bu, L.; Shao, Q.; Huang, X. Structurally Ordered Pt_3Sn Nanofibers with Highlighted Antipoisoning Property as Efficient Ethanol Oxidation Electrocatalysts, *ACS Catalysis*, **2020**, *10*, 3455–3461. Copyright 2020 American Chemical Society.

ability of Pt_3Sn catalyst to resist CO-poisoning but as well as the further improvement due to the aspect ratio effect.[14]

On the other hand, a study conducted by Chen et al.[40] showed that a 2D-nanomaterial of sub-1-nm PtSn hexagonal-ultrathin sheet exhibited better activity and durability compared to commercial Pt black and Pt/C catalysts for AOR (Table 1, Entry 14). It is suggested that the enhanced property is correlated to the exposure of the highly-reactive Pt(111) facet sites that were brought about by the sub-1 nm 2D sheet like morphology as shown in the simulation (Figure 11).

3. Mechanistic Studies Based on Advanced *in Situ* and *in Operando* Techniques

In the previous paragraphs, it has been shown that Sn is able to impart both increased performance and stability to Pt based electrocatalysts. An in depth understanding of this synergistic effect and of the reactions involved can be achieved through the implementation of *in situ/operando* spectroscopic and analytical techniques.

It is worth to emphasize here that while the *in situ* and *in operando* techniques may coincide, they refer to two different types of experiments. In the first case, *in situ* refers to data collection of the catalyst, for example its synthesis, or post-treatment (calcination, activation etc.). In the second case, the catalyst is monitored while being under working conditions, i.e. while measuring its performance. An overview of the most widely used *in situ/operando* methodologies is reported in Scheme 2. Additionally, Table 2 summarizes the *in situ/operando* studies carried out on thermal and electrochemical nano-catalysts and single crystal surfaces based on the PtSn system.

3.1. Infrared Spectroscopy

Infrared spectroscopy was among the first techniques to be implemented to study electrochemical reactions under *in operando* conditions. Hence, nowadays, potential dependent FTIR spectroscopy is a state-of-the-art technique in electrochemistry. Few examples of these studies have been mentioned in the paragraph 2.3 of this Perspective to account for the fundamental steps of the anodic oxidation of hydrogen, carbon monoxide, and H_2/CO mixtures and the promotion effect of Sn/SnO_2 in PtSn electrocatalysts.[15,33,44,49] For the electrochemical oxidation of ethanol, the positive bands at 2987 and 2908 cm^{-1} are associated to CH_3 and CH_2 groups from the ethanol consumption. Negative bands are related to species that

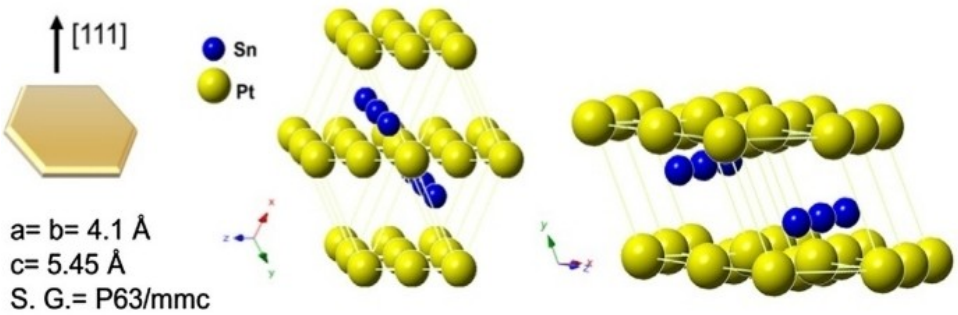

Figure 11. Simulation structure of sub-1-nm PtSn hexagonal-ultrathin sheet.[40] This figure was published in *Journal of Colloid and Interface Science*, 545, Jee-Yee Chen, Suh-Ciuan Lim, Chun-Hong Kuo, Hsing-Yu Tuan, Sub-1 nm PtSn ultrathin sheet as an extraordinary electrocatalyst for methanol and ethanol oxidation reactions, 54–62, Copyright Elsevier (2019)

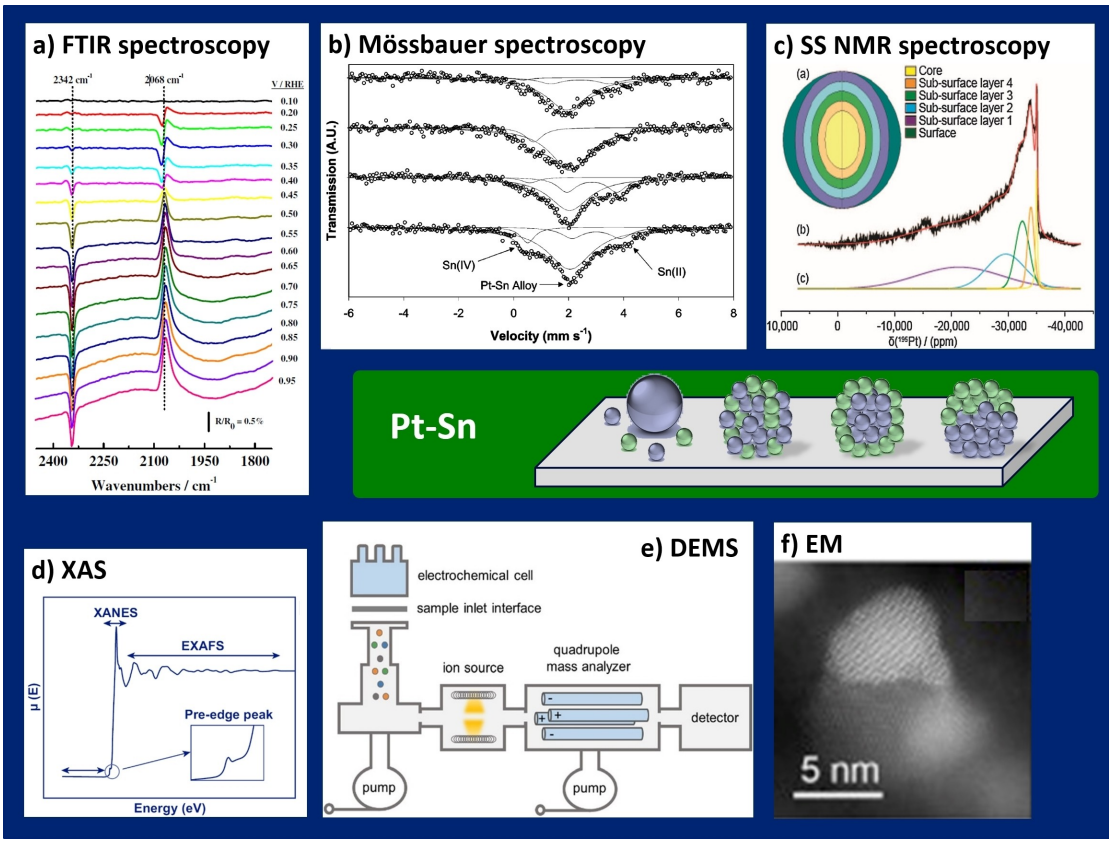

Scheme 2. Overview of the *in situ/operando* techniques for the advanced characterization of PtSn nanoparticles. a) Potential dependent Fourier Transform Infrared (FTIR) spectroscopy.[48] This figure was published in *International Journal of Hydrogen Energy*, 37, T. Herranz, S. García, M. V. Martínez-Huerta, M. A. Peña, J. Fierro, F. Somodi, I. Borbáth, K. Majrik, A. Tompos and S. Rojas, Electrooxidation of CO and methanol on well-characterized carbon supported PtxSn electrodes. Effect of crystal structure, 7109–7118, Copyright Elsevier (2012). b) Mössbauer spectroscopy. Reprinted with permission from Alcala, R.; Shabaker, J. W.; Huber, G. W.; Sanchez-Castillo M. A.; Dumesic, J. A. Experimental and DFT studies of the conversion of ethanol and acetic acid on PtSn-based catalysts, *J. Phys. Chem. B* **2005**, *109*, 2074–2085. Copyright 2005 American Chemical Society. c) Solid State Nuclear Magnetic Resonance (SS NMR spectroscopy). Reproduced from Ref. [50] with permission from the Royal Society of Chemistry. d) X-ray Absorption Spectroscopy (XAS) and its modification. Reproduced under terms of the CC-BY license. Copyright (2019), Maoyu Wang et al., published by Springer. e) Differential Electrochemical Mass Spectrometry (DEMS). Reproduced from Ref. [52] with permission from the Royal Society of Chemistry. f) Electron Microscopy characterization. This figure was published in *Chem*, 5, T. Ma, S. Wang, M. Chen, R. V. Maligal-Ganesh, L.-L. Wang, D. D. Johnson, M. J. Kramer, W. Huang and L. Zhou, Toward Phase and Catalysis Control: Tracking the Formation of Intermetallic Nanoparticles at Atomic Scale, 1235–1247, Copyright Elsevier (2019).

undergo formation and they can be assigned as reported in Table 3.[71]

To avoid the appearance of the sulfate stretching vibration, perchlorate electrolyte can be used, instead.[71]

Magalhães et al. studied the electrooxidation of ethanol onto the surface of Pt_3Sn, Pt_3Cu and PtSnCu nanoalloys supported onto carbon substrate using a combination of cyclic voltammetry and FTIR spectroscopy.[55] PtSnCu/C and Pt_3Cu/C started to produce CO_2 at 0.70 V vs. RHE, while this product was detected only at 0.75 V and 0.80 V vs. RHE on Pt and Pt_3Sn/C, respectively, suggesting that Cu improves the dissociative adsorption of ethanol.[55]

Colmati et al. observed that the amount of CO and consequently of CO_2 produced during the ethanol oxidation on Pt(111), Pt(100) and Pt(110) electrodes was very small and probably associated with the defects present on the electrode surface. The authors suggested that the C–C bond splitting on the Pt(111) surface is only possible in the presence of surface defects.[54]

3.2. Mössbauer Spectroscopy

Mössbauer spectroscopy provides quantitative information about the chemical and spin state, and on the coordination symmetry of some selected elements such as Fe, Sn, Ru, Au etc. present in the catalysts. The Mössbauer effect is due to the recoilless emission and absorption resonance of the γ-rays used to irradiate the sample. The Mössbauer spectra contain three important parameters, i.e. the isomer shift (IS), the quadrupole splitting (QS), and the magnetic hyperfine field (B). The Coulomb interaction between the nucleus and the s-electrons determine the electronic structure of a given element and its isomer shift (IS). The IS provides information such as chemical state, spin state and electronegativity of coordination groups. The quadrupole splitting QS derives from the electric quadrupole moment interaction between the quadrupole moment of the nucleus and the electric field gradient caused by the extranuclear environment. QS can provide the electronic symmetry

Table 2. Summary of the *in situ* studies on PtSn systems using the techniques shown in Scheme 2.

Catalysts	Reaction	*In situ* technique	Conclusions	Ref.
Pt(111), Pt(100) and Pt(110)	EthOH Ox	Electrochemical and FTIR	C–C bond splitting occurs at defects	[54]
Pt_3Sn/C, Pt_3Cu/C and PtSnCu/C alloys	EthOH Ox	CV and FTIR spectroscopy	Cu improves the dissociative adsorption of ethanol	[55]
PtSn/C, PtSn/SiO_2, PtSn/MgO, PtSn/Al_2O_3	Dehydrogenation of light alkanes	^{119}Sn-Mössbauer spectroscopy	In PtSn/Al_2O_3, a stable layer of Sn(II) aluminate forms	[56,57]
PtSn/SiO_2	Dehydrogenation of EthOH to acetaldehyde	^{119}Sn-Mössbauer spectroscopy and DFT calculations	PtSn inhibits the decomposition of ethanol to CO, CH_4 and C_2H_6.	[49]
Pt-rich- and Sn-rich- PtSn catalyst on SiO_2	CO Ox	FTIR and ^{119}Sn-Mössbauer spectroscopy	Formation of intermediate Sn oxides species	[58]
PtSn alloy/SiO_2 with traces of Sn	Dehydrogenation of EthOH	^{119}Sn-Mössbauer spectroscopy	Sn changes between (II) and (IV)	[49]
PtSn NPs/CeO_2 and PtSn NPs/(CeO_2- Al_2O_3)	Hydrogenation of crotonaldehyde to crotyl alcohol	^{119}Sn-Mössbauer spectroscopy, XPS and micro-calorimetry	Sn and/or CeO_2 added to Pt/Al_2O_3 leads to higher selectivity	[59]
Pt nanoclusters, PtSn IMs, and Pt_3X alloys (X=Al, Sc, Nb, Ti, Hf and Zr)	ORR	^{195}Pt NMR spectroscopy	The mean number of Pt atoms in a NP and in each layer from the surface can be accurately determined	[50]
Sn, Pt and PtSn clusters onto TiO_2 (110), rutile	Particle formation study	XPS	Low surface coverage: SnO_x; High surface coverage: Sn^0 clusters.	[60]
Pt_3Sn (111)	Particle formation study	AP-XPS	SMSI occurs, Pt_3Sn is covered by a layer of SnO	[61]
PtSn NPs *vs* Pt NPs	CO Ox to CO_2	AP-XPS	Pt and Sn are mobile within NPs; SnO forms first and is then reduced to Sn by CO	[62]
Flat Pt(111) and stepped Pt(223) single crystal surfaces	CO Ox	Near AP-XPS	Up to 200 °C, SnO onto Pt(111) and SnO_2 onto Pt(223); Above 300 °C, SnO on edges are reduced to Sn^0	[63]
Pt_3Sn catalyst vs Pt	PROX	XPS at synchrotron radiation	Higher activity of Pt_3Sn; during PROX, Sn present as $Sn.^0$	[64]
Pt_3Sn vs Pt supported on graphite	EthOH Ox	Cyclic Voltammetry and QXANES	Dynamic dissociative adsorption of EthOH onto PtSn surface.	[65]
PtSn alloys and IMs	Particle formation study	*in situ* X-ray scattering	• reduction of Pt(II) to Pt; • fast Sn diffusion into Pt; • fast reordering (300 s) of Pt and Sn into PtSn IMs at around 280 °C	[45]
Pt(110) and Pt(111) surface	MeOH Ox	DEMS	Pt(110) > Pt(111) > Pt(332);	[66]
hcp PtSn and fcc Pt_3Sn IMs	MeOH and CO Ox	cyclic voltammetry, infrared spectroscopy and DEMS.	• Reactivity fcc Pt_3Sn > hcp PtSn; • PtSn less active and more selective towards CO_2.	[48]
Pt- and Sn-decorated mesoporous Pt *vs* commercial Pt_3Sn/C catalyst	MeOH Ox	DEMS	Mesoporous Pt could replace carbon-supported materials in low temperature fuel cells	[67]
Pt/C, PtRu/C and Pt_3Sn/C electrodes	EthOH Ox	FTIR and DEMS	• Ru and Sn increase the activity of Pt catalyst; • Main products are $CH_3C(O)H$ and $CH_3C(O)OH$; • CO_2 < 2% of the total current.	[68]
PtSn/C vs PtSn/TiC	EthOH Ox	FTIR and DEMS	PtSn/TiCN leads to acetaldehyde, reducing Pt poisoning	[69]
Pt and SnO_2 in mesoporous SiO_2	Solid-state rearrangement of Pt and Sn atoms	HAADF-STEM and MD simulations	Consecutive formation of Pt_3Sn and PtSn ordered phases.	[53]
PtSn@mSiO_2	Hydrogenation of furfural to furfuryl alcohol	TEM and HAADF-STEM	Reversible phase separation occurs, due to Sn→ SnO_2 reaction.	[70]

CV = cyclic Voltammetry; FTIR = Fourier Transform Infrared Spectroscopy; XPS = X-ray Photo-absorption Spectroscopy; SMSI = Strong Metal Support Interaction; AP = Ambient Pressure; PROX = Preferential Oxidation of CO in excess hydrogen; QXANES = Quick X-ray Absorption Near Edge Spectroscopy; HAADF-STEM = High-Angle Annular Dark-Field Scanning Transmission Electron Microscopy; TEM = Transmission Electron Microscopy.

of atoms. Finally, the magnetic hyperfine field B is caused by magnetic dipole interactions within the nucleus.[72]

Mössbauer spectroscopy has been widely used as ex-situ characterization tool to understand the interaction of Pt with Sn in various catalytic thermal processes. In an early study, the

Table 3. Assignment of the main vibrations observed by *in situ* FTIR spectroscopy.

Wavenumbers/cm^{-1}	Functional group/molecule	Vibration mode
2343 cm^{-1}	CO_2	$\nu_{O=C=O}$ asym.
2050 and 1850 cm^{-1}	adsorbed CO on Pt	ν_{CO} linear and bridge configuration, respectively
1713 cm^{-1}	acetic acid and/or acetaldehyde species	$\nu_{C=O}$
1398 cm^{-1}	CH_3COO- on Pt	$\nu_{C-O\ asym}$
1368 and 1280 cm^{-1}	acetic acid	coupled $\nu_{C-O} + \delta_{O-H}$ of COOH group
1353 cm^{-1}	acetaldehyde and/or acetic acid	δ_{CH3}
1190 cm^{-1}	adsorbed sulfate species from the electrolyte	ν_{SO4}

oxidation states of Sn in PtSn catalysts supported onto activated carbon, silica, MgO and Al_2O_3 after the dehydrogenation of light alkanes was investigated. For $PtSn/Al_2O_3$ catalyst, it was observed that Sn^{2+} formed after reduction interacts very strongly with the Al_2O_3 surface forming a stable layer of Sn(II) aluminate that stabilizes the catalyst upon interaction with Pt.[56,57]

In situ Mössbauer spectroscopy, in combination with DFT calculations, was used to demonstrate that the addition of Sn to Pt inhibits the decomposition of ethanol to CO, CH_4 and C_2H_6. At temperatures from 500 to 600 K, the $PtSn/SiO_2$ catalyst was very selective for the dehydrogenation of ethanol to acetaldehyde.[49] The combination of FTIR and Mössbauer spectroscopy revealed that the room temperature oxidation of CO implies the formation of intermediate species based on Sn oxides, and of a third alloy species of PtSn (1 : 1), starting from a mixture of Pt-rich- and Sn-rich- PtSn catalyst supported on silica.[58]

Some authors could shed light more specifically onto the oxidation state of the Sn, when present in its oxidized form. Interestingly, *in situ* Mössbauer spectroscopy showed that while the PtSn alloy supported on silica remains intact during the dehydrogenation of ethanol, the traces of Sn present in the electrocatalyst as ionic species undergo dynamical changes between the oxidation state (II) and (IV).[49]

Mössbauer spectroscopy was combined with X-ray Photo-Absorption Spectroscopy (XPS) and micro-calorimetry to shed light on the strong metal support interaction (SMSI) occurring between PtSn nanoparticles and two different substrates, i.e. CeO_2 and CeO_2/Al_2O_3, during the hydrogenation of crotonaldehyde to crotyl alcohol. The results show that the reduction of Sn was inhibited by the presence of Ce, and that Ce was preferentially found in its reduced state as Ce(III).[59]

In conclusion, *in situ* Mössbauer spectroscopy is well documented in the literature for thermal processes making use of PtSn catalysts supported on various materials (AC, SiO_2, Al_2O_3, CeO_2, etc.). On the contrary, for electrochemical processes this technique appears to be less investigated. While *in operando* Mössbauer spectroscopy has been already used to characterize Sn-based electrodes in batteries, the characterization of Sn-based electrocatalysts under working conditions appears scarce. While this is a knowledge gap, it represents as well as a possibility for future in depth studies making use of ^{119}Sn-Mössbauer spectroscopy. An overview of the *in situ/operando* Mössbauer spectroscopy to characterize heterogeneous catalysts and materials has been recently published by Zheng et al.[73]

3.3. Solid State Nuclear Magnetic Resonance (SS NMR)

NMR spectroscopy has been widely explored in the field of materials characterization to elucidate the structure, composition and in some cases the functioning of materials. This technique is based on the interaction of magnetic dipoles with an applied magnetic field and electromagnetic radiation of suitable wavelength. In NMR spectroscopy, the magnetic dipole arises from the splitting of nuclear magnetic spin coupled with the protons and neutrons present in the nuclei. Catalysts and electrocatalysts based on PtSn are potentially interesting materials to be characterized by NMR spectroscopy. The magnetically active^{195}Pt isotope has a natural abundancy of 33.8% and a nuclear spin of 1/2. Due to the very large anisotropic interactions that exist in the solid state, the line shapes of ^{195}Pt are very broad ($>$3 MHz), making SS NMR a seldom used characterization technique for Pt based materials. On the contrary, solution studies are more common, as the rapid molecular rotation effectively averages the anisotropic effects. On the other side, Sn has three stable NMR active isotopes, with nuclear spin of 1/2 (^{115}Sn, ^{117}Sn, ^{119}Sn). Like ^{195}Pt NMR, ^{119}Sn has a large chemical shift range. Rees et al used the Field Sweep Fourier Transform (FSFT) method to acquire ^{195}Pt NMR spectra from Pt_{13} nanoclusters and PtSn intermetallic nanoparticles (Scheme 2 c).[50] With the exclusion of this paper, the literature making use of NMR spectroscopy to characterize PtSn nanoparticles is very limited, to the best of our knowledge.

The next paragraphs focus on more advanced techniques, which were implemented more recently, both to better understand the formation of PtSn nanoparticles at atomic scale, and to monitor their functioning under *in operando* conditions.

3.4. X-ray Based Techniques

X-rays are electromagnetic radiation with energies ranging from about 200 eV to 1 MeV, which include them between γ-rays and ultraviolet (UV) radiation in the electromagnetic spectrum. X-ray based techniques are among the most widespread method-

ologies for catalysts characterization, therefore they are widely documented in the literature also for catalyst systems based on PtSn. To give an overview of the results, the corresponding papers are organized based on the physical principle of interaction of X-rays with matter.

3.4.1. X-ray Photoelectron Spectroscopy (XPS)

XPS is a surface analysis technique based on the photoelectric effect discovered in 1887 by Heinrich Hertz. In this technique, the surface of materials is irradiated with soft X-rays (energy < 6 keV) and the kinetic energy of the emitted electrons is measured. It gives information about the surface (ca. 10 nm) and the chemical environment of the elements. Normally, XPS is measured under ultra-high vacuum, therefore the materials are characterized under experimental conditions that are very different from those typically employed in catalysis (i.e. high temperature and pressure, presence of a liquid phase, etc.). This limitation is known as *pressure gap*. Additionally, the majority of studies is conducted using single crystal surfaces where the elementary processes of adsorption of reagents, their reaction or chemical rearrangement, and the product desorption can be understood at atomic and molecular scale. However, the chemical and physical properties of industrial catalysts deviate remarkably from the well-defined properties of single-crystal surfaces. This limitation is known as *material gap.* In the emerging field of environmental or ambient pressure XPS (AP-XPS), measurements are carried out under near ambient pressure (up to 25 mbar), and low volatile liquids as well as catalysts under working conditions can therefore be analysed.[74,75]

Conventional XPS has been largely used to foster the rational design of PtSn thermal- and electrocatalysts and shed light on particle formation. Beniwal et al. investigated in depth the behaviour of Sn, Pt and PtSn clusters deposited onto the surface of rutile TiO_2 (110).[60] The authors found that the chemical nature of Sn clusters depends on the surface coverage: for low surface coverages, the clusters are evenly distributed and Sn is present as SnO_x at the interface with TiO_2.[60] For larger surface coverage, the intensity of the Sn^0 peak increases, indicating the formation of Sn^0 clusters. Concerning the bimetallic PtSn, the incorporation of Pt into the existing Sn clusters results in an increase in metallic Sn at the expenses of SnO_x, with formation of a PtSn alloy. At the same time, Ti^{4+} is reduced by the presence of Sn, to Ti^{n+}, with $n < 4$.[60]

Jugnet et al. filled the pressure gap, but not the material gap. They observed that Pt_3Sn (111) surfaces form SnO, PtO, SnO_2 and PtO_2 under oxygen atmosphere, and observed the adsorption of CO_2 onto the bimetallic system under conditions of co-adsorption of oxygen and CO (as bridge species). Under optimum catalytic conditions, the surface of Pt_3Sn is covered by a layer of SnO.[61] Using AP-XPS, Michalak et al. demonstrated that Pt and Sn atoms are mobile within nanoparticles. The high resistance to CO poisoning of PtSn- with respect to Pt-nanoparticles is due to the reaction of oxygen with Sn, to form first SnO, which is subsequently reduced to Sn by CO.[62] In the presence of CO, the PtSn nanoparticles evolved from an intermixed system of Pt and Sn domains, to isolated domains of Pt and SnO within the single nanoparticles.[62] The authors measured as well a change in the activation energy from 133 kJ/mol in case of Pt nanoparticles to 35 kJ/mol in case of PtSn nanoparticles.[62] The oxidation of CO to CO_2 occurs at the interface between Pt and SnO domains,[62] as also confirmed by DFT calculations.[76] Using flat Pt(111) and stepped Pt(223) single crystal surfaces, Wallander et al. could conclude that up to 200 °C, Sn is present as SnO layer onto the surface of Pt(111) and as 3D clusters of SnO_2 onto the Pt(223). At temperature above 300 °C, only the Sn(II) oxides possessing edge sites can be reduced to Sn^0 species both as isolated and alloyed species, by the presence of CO adsorbed preferentially onto Sn(II) surfaces. The continuous layers of SnO do not undergo reduction.[63]

Teschner et al studied the preferential oxidation of CO in excess hydrogen (PROX) over an unsupported PtSn catalyst using *in situ* XPS at synchrotron radiation.[64] The PROX reaction is a valuable approach to produce H_2 streams with the 10 ppm CO limit required for proton exchange membrane fuel cell (PEMFC) applications.[77] The results are interesting for a better understanding of the structure-function property of PtSn catalysts. In fact, in a first instance, the authors confirmed a higher activity of Pt_3Sn catalyst against Pt. *In situ* XPS showed that Pt was present in its elementary state as Pt^0, with a small shift of the binding energy, as consequence of the alloying. Sn was present preferentially as oxide after H_2 and O_2 pre-treatment, but during PROX, Sn was mainly present as Sn^0, with 40 % present as Sn oxides, indicating that besides small surface islands, the PtSn bimetallic structure was preserved during PROX reaction.[64]

3.4.2. X-ray Absorption Spectroscopy (XAS)

In XAS, core electrons are excited to unoccupied states when the energy of the incident X-ray beam is larger than the binding energy of the electron in the element's orbital (Scheme 2d). For sufficiently high energy, a strong absorption of the X-ray occurs which corresponds to the X-ray absorption near edge structure (XANES) and contains information about the valence state and the chemical environment of the core electrons. The low intensity features that appear in the X-ray absorption spectra immediately before the XANES are low probability transitions occurring at low energy of the incident beam (pre-edge peaks, inset in Scheme 2d). For higher energy of the X-rays, the electrons undergo constructive or deconstructive scattering wave interferences with neighbour atoms, called extended X-ray absorption fine structure (EXAFS). The EXAFS region of a XAS spectrum contains information about the local atomic structure such as bond distance and coordination numbers.[51]

Quick X-ray absorption spectroscopy (QXAS), in particular quick X-ray-absorption near-edge structure (QXANES) spectrum, has a time resolution down to microseconds, therefore it appears suitable to follow the fast dynamics occurring onto the electrocatalyst surfaces.[51] Su et al. utilized QXANES to monitor

the evolution of the electronic structure and the valence of Pt in Pt_3Sn and Pt supported on graphite during the anodic scan of cyclic voltammetry for the ethanol oxidation reaction. They observed that the white-line intensities of the Pt L3-edge QXAS spectra vary remarkably with the electrode voltage as a consequence of a dynamic dissociative adsorption of ethanol onto the surface of PtSn electrocatalysts (Figure 3).[65]

3.5. Differential Electrochemical Mass Spectrometry (DEMS)

DEMS enables the simultaneous analysis of mass-, potential-, space- and time-resolved signals of electrochemical reactions with high sensitivity and specificity. Both gaseous and volatile species generated at the solid/liquid interface of the electrodes are detected in real time.[52] Upon mass and potential calibration, DEMS can be used for quantitative studies and in contrast with electrochemical methods such as voltammetry and impedance spectroscopy, it provides direct evidence of the molecular species involved in electrochemical transformations. Accordingly, DEMS has been used to shed light on the mechanism of electrochemical reactions underpinning DAFCs. For example, it has been shown that Pt(110) is the most active surface for the electrochemical oxidation of methanol, whereas the Pt(111) surface is the least reactive. However, the rate of methanol oxidation can be increased by increasing the step density onto Pt(111) surfaces. This has been assessed by comparing the corresponding DEMS results of the oxidation of methanol to CO_2 onto Pt(111) and Pt(332) single crystals, whereby the latter is about six times more reactive than the former.[66]

Herranz et al. studied the reactivity of hcp PtSn and the fcc Pt_3Sn intermetallic catalysts in the electrooxidation of methanol and CO using *in operando* cyclic voltammetry, infrared spectroscopy and DEMS.[48] The authors concluded that the fcc Pt_3Sn was more active in both reactions, whereas PtSn was less active and more selective towards CO_2.[48] The lower reactivity of the PtSn system was attributed to the dilution of the active centers responsible for the methanol adsorption and dehydrogenation reaction. Such active centers comprise three Pt neighboring atoms, and their occurrence in the structure decreases with increasing the Sn content.[48] However, the onset potentials for the appearance of CO_2 and the signal $m/z = 44$ during the electrooxidation of CO_{ad} are very similar on both hcp PtSn and fcc Pt_3Sn electrodes indicating that Sn promotes the nucleation of OH species independent of its loading.[48] The authors identified also methylformate, a key intermediate in the electrochemical oxidation of methanol, which also contribute to the $m/z = 44$ signal.[48] Flórez-Montano et al compared the efficiency of methanol electrooxidation onto as-prepared- and Sn-decorated mesoporous Pt electrodes and compared it with commercial Pt_3Sn/C catalyst. The authors found that the CO_2 signal at $m/z = 44$ at 0.55 and 0.65 V at 25 °C depends on the catalytic nature of the electrode and increases going from Pt_3Sn/C (E-TEK), to mesoporous Pt, to mesoporous platinum decorated with Sn. The methanol conversion to CO_2 was almost complete onto the Pt–Sn electrode at 0.55 V, whereas at higher potential formaldehyde formed as side product, reducing the total amount of CO_2 and consequently the faradaic current. Therefore, the authors conclude that the mesoporous electrodes of Pt could replace carbon supported materials in low temperature fuel cells, to overcome the carbon corrosion that leads to dissolution and agglomeration of the catalyst, and subsequent loss of fuel cell performance.[67]

Concerning DEFCs, DEMS studies confirm that acetaldehyde is a key intermediate in the dissociative adsorption of ethanol onto Pt electrodes, whereas acetic acid cannot be detected due to its higher vapour tension. DEMS and FTIR are complementary techniques to understand the mechanism of ethanol electrooxidation on Pt/C, PtRu/C and Pt_3Sn/C. The addition of Sn or Ru, though beneficial for the overall activity for ethanol oxidation, does not promote the C–C bond breaking. The dissociative adsorption of ethanol to form CO_2 is easier on Pt/C catalyst rather than on PtRu/C and Pt_3Sn/C catalysts for potentials lower than 0.6 V, but Pt/C is rapidly poisoned by the CO adlayer. In all cases, acetaldehyde and acetic acid are the dominant products, and CO_2 account for less than 2% of the total current. The higher ethanol oxidation current density on the Pt_3Sn/C catalyst at these potentials results from higher yields of C2 products, not from an improved complete ethanol oxidation to CO_2.[68]

A combination of DEMS and *in situ* FTIR spectroscopy was used to shed light on the influence of support on the catalytic activity of PtSn NPs in the electrooxidation of ethanol. For PtSn NPs deposited onto carbon Vulcan, the onset potential for the formation of CO was detected at 0.30 V, against 0.27 V observed for PtSn NPs deposited onto TiCN. A more remarkable difference was observed for the formation of CO_2, which was much faster for PtSn/TiCN catalyst. At the same time, the *in situ* FTIR spectra show that at potentials higher than 0.5 V, PtSn/C shows bands associated to the formation of acetaldehyde, acetic acid and acetate, whereas in the meanwhile PtSn/TiCN mainly displays the band related to the production of acetaldehyde, reducing the platinum surface poisoning.[69]

3.6. *In situ* Electron Microscopy

Using High-Angle Annular Dark-Field Scanning Transmission Electron Microscopy (HAADF-STEM), Ma et al. directly monitor the rearrangement of atoms during a solid-state reaction between nanocrystalline Pt and SnO_2 encapsulated in a shell of mesoporous silica. They observed the consecutive formation of Pt_3Sn and PtSn ordered phases.[53] The particle formation was triggered by the electron beam, which acted as a sub-angstrom electron probe and induced first the fast reduction of SnO_2, followed by the surface diffusion of Sn around the Pt domains.[53] The high contrast shell around the Pt domains was assigned to Pt_3Sn and by increasing the irradiation time the nucleation of PtSn onto the Pt_3Sn surface was observed (Scheme 2 e). The driving force for the transformation of the Pt_3Sn phase into PtSn was the interfacial structure of Pt_3Sn/PtSn, which induces tensile stress on the Pt atoms and promoted the substitution of Pt by Sn. The authors coupled the

experimental observations with Molecular Dynamic (MD) simulations.[53]

The high stability of PtSn-intermetallics during the ORR reported in Figure 5 is not necessarily maintained if this material system is exposed to high temperature conditions. For example, PtSn nanoparticles encapsulated in a mesoporous silica shell ($PtSn@mSiO_2$) are excellent catalysts for the hydrogenation of furfural to furfuryl alcohol, however they promptly undergo deactivation due to the formation of carbon deposits. Calcination in air can effectively remove the carbon deposits, however this step leads to a dramatic catalyst deactivation. The catalyst can be regenerated in hydrogen atmosphere at 350 °C (Figure 12 a). Both the calcination and the regeneration are accompanied by a dramatic restructuring of the particle cores, as demonstrated by *in situ* Transmission Electron Microscopy (TEM) and HAADF-STEM elemental map analysis (Figure 12 b). While Pt and Sn in the initial intermetallic nanocatalysts are homogeneously distributed, the calcination step leads to a phase separation within the particle cores. The phase separation is due to the transformation of elemental Sn into SnO_2. The homogeneous distribution of Pt and Sn within the particle core is achieved upon the regeneration step, which reduces the SnO_2 back to Sn (Figure 12 b) and leads to a complete recovery of the catalytic activity.[70] This study is a nice example of structure-function property in catalytic materials using advanced *in situ* microscopy.

4. PtSn as a Parent System for High Entropy Alloys and Intermetallics

With the plethora of synthetic methodologies developed to prepare a large variety of binary intermetallic nanocrystals, recently the attention of the scientific community shifted towards the incorporation of more than two elements in monometallic nanocrystals to form ternary or even multinary intermetallic nanocrystals. As an example, Li et al. prepared PtCoM (M═Mn, Fe, Ni, Cu, and Zn) ternary intermetallic nanocrystals, and identified the PtCoNi as the most active ORR catalyst.[78] When there are at least five chemical elements with nearly equal atomic ratio, it is possible to obtain either high entropy alloys (HEA) or high entropy intermetallic materials (HEI), according to the disordered or ordered arrangement of the constituent elements, respectively.[7] The specific crystal structure of HEIs depends on the parent bimetallic counterpart. More specifically, each metal in the bimetallic nanocrystal is substituted with at least one element with analogous characteristics (radius, electronegativity). Xing et al. have recently reported that the HEI (PtCoNi)(InGaSn) supported onto CeO_2 acts as an efficient catalyst for the oxidative dehydrogenation of propane using CO_2.[79] The structure of this catalyst can be understood starting from the binary intermetallic PtSn, upon partial substitution of Pt atoms with Co and Ni, and of Sn atoms with In and Ga atoms (Figure 13). Co and Ni have a higher ability to activate CO_2, and additionally increase the Pt–Pt distance improving the selectivity of the reaction. On the other side, In and Ga increased the entropy of the system and provided thermodynamic stability.[79]

While the field of PtSn-based HEIs as electrocatalysts remains mostly unexplored, the use of HEIs containing both Pt and Sn appears certainly interesting. For example, Chen et al. reported the one-pot synthesis of PtRhBiSnSb HEI nanoplates with intrinsically isolated Pt, Rh, Bi, Sn, and Sb atoms. The authors demonstrated that the as-synthesized material acts as efficient electrooxidation catalyst of methanol, ethanol, and glycerol in alkaline electrolytes.[80]

The synthesis and (electro)catalytic application of HEAs and HEIs is just at its infancy, and it is advisable that the earth abundant and cheap element Sn will play a pivotal role as electrocatalyst component in the coming years.

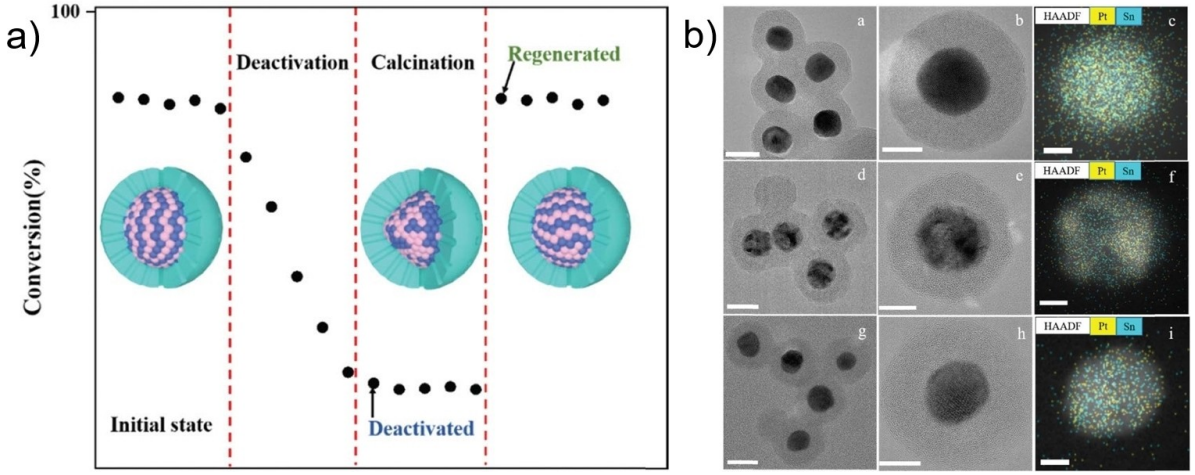

Figure 12. a) Scheme of the catalytic activity changes of $PtSn@mSiO_2$ catalysts during the reaction process. b) TEM images and HAADF-STEM elemental distribution of Pt and Sn in the $PtSn@mSiO_2$ iNPs after different treatments. The initial state (a, b and c), after decarbonization (d, e and f) and after regeneration (g, h and i). Scale bars: 20 nm in a, d and g; 10 nm in b, e and h; 5 nm in c, f and i. HAADF-STEM: c, f and i; yellow spots: Pt, blue spots: Sn. Reproduced from Ref. [70] with permission from the Royal Society of Chemistry.

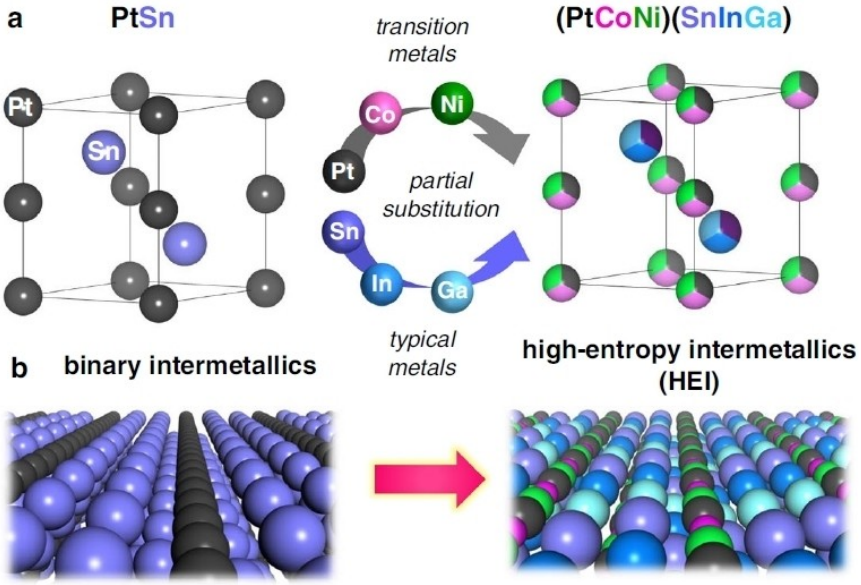

Figure 13. Design of HEI catalyst based on PtSn intermetallics, where the Pt and Sn sites are partially substituted by Co/Ni and In/Ga, respectively, forming a PtSn-type HEI (PtCoNi) (SnInGa). Reproduced under terms of the CC-BY license.[79] Copyright (2022), Feilong Xing et al., published by Springer Nature.

5. Summary and Outlook

Based on the literature reviewed, aspect ratio, shape and alloy content affect the performance of PtSn nanocatalyst, which are reflected to the structural and electrochemical results. Higher aspect ratio provides more stability due to the structure's ability to resist degradation and aggregation. The formation of intermetallic is preferable to alloying, as it improves the catalyst performance via increasing resistance to poisoning from CO and related intermediates. Exposure of specific facets such as Pt(111), can significantly increase the catalyst performance due to its higher activity during electrocatalysis. However, there is a maximum amount of Sn to obtain the optimum activity, which can be determined from the volcano type relationship of cell potential versus % Sn content. The formation of Sn-oxides also enhances the activity as demonstrated by comparing two PtSn with the same Pt:Sn ratio but different SnO_2 content. *In situ* and *in operando* analytical and spectroscopic techniques are an ensemble of established and advanced characterization methodologies that, both alone and in combination, shed light on the elementary steps of formation and functioning of materials, including catalysts and electrocatalysts. Their implementation has the potential to boost the material development through rational design rather than by trial-and-error.

In general, PtSn bimetallic system is a promising catalyst due to its versatility. It can be used as an anode catalyst due to its ability to overcome poisoning from CO and related intermediates. As a cathode catalyst, it makes the ORR proceed at a faster rate. On top of these, Sn is the 49th most abundant element on the earth crust and therefore it is much cheaper than the elements in the PMG used until now to alloys Pt in PtM bimetallic nanocatalysts. Providing that the international trade of this element is strictly regulated, Sn has the potential to play a pivotal role as electrocatalyst component in the next years. For example, PtSn bimetallic material can serve as parent system for the synthesis of high entropy alloys and intermetallics, opening a completely new era in the field of supply-risk-free catalysts for sustainable electromobility.

Author Contributions

EA wrote the first version of the paper, MD conceived, wrote and finalized the paper. Both authors have read and agreed on the final version of the manuscript.

Acknowledgements

This work received no funding. Open Access funding enabled and organized by Projekt DEAL.

Conflict of Interests

The authors declare no conflict of interest.

Keywords: Alloys · Intermetallics · Nanoparticles · Mobility · sustainability

[1] K. K. Karuppanan, M. K. Panthalingal, P. Biji, *Handbook of Nanomaterials for Industrial Applications*, Elsevier, **2018**, 468–495.
[2] R. L. Borup, Ahmet Kusoglu, K. C. Neyerlin, R. M. R. K. Ahluwalia, D. A. Cullen, K. L. More, A. Z. Weber, D. J. Myers, *Curr. Opin. Electroche* **2020**, *21*, 192–200.
[3] World Platinum Investment Council, Fuel cell electric vehicles and platinum demand, https://www.cmegroup.com/articles/2022/wpic-fuel-cell-electric-vehicles-and-platinum-demand.html, (accessed on February 2024).

[4] J. Yan, J. Jing, Y. Li, *Int. J. Hydrog. Energy* **2024**, *52*, 734–749.
[5] P. Ghosh, *Clean Technologies and Environmental Policies* **2017**, *19*, 595–601.
[6] EU, Conflict Minerals Regulation: The regulation explained, https://policy.trade.ec.europa.eu/development-and-sustainability/conflict-minerals-regulation/regulation-explained_en.
[7] J. Liu, C. Lee, Y. Hu, Z. Liang, R. Ji, X. Y. D. Soo, Q. Zhu, Q. Yan, *SmartMat* **2023**, *4*, e1210. DOI: 10.1002/smm2.1210.
[8] Y. Wang, Y. Pang, H. Xu, A. Martinez, K. S. Chen, *Energy Environ. Sci.* **2022**, *15*, 2288–2328.
[9] W. Zhang, X. Fang, C. Sun, *J. Environ. Manage* **2023**, *341*, 118019.
[10] D. Teichmann, W. Arlt, P. Wasserscheid, R. Freymann, *Energy Environ. Sci.* **2011**, *4*, 2767.
[11] G. Sievi, D. Geburtig, T. Skeledzic, A. Bösmann, P. Preuster, O. Brummel, F. Waidhas, M. A. Montero, P. Khanipour, I. Katsounaros, J. Libuda, K. J. J. Mayrhofer, P. Wasserscheid, *Energy Environ. Sci.* **2019**, *12*, 2305–2314.
[12] P. Preuster, C. Papp, P. Wasserscheid, *Acc. Chem. Res.* **2017**, *50*, 74–85.
[13] S. Nahal Aramesh, *Inorg. Chem.* **2020**, *59*, 10688–10698.
[14] Y. Zhu, L. B. Qi, X. H. Shao, *ACS Catal.* **2020**, *10*, 3455–3461.
[15] V. K. Puthiyapura, D. J. L. Brett, A. E. Russell, W.-F. Lin, C. Hardacre, *ACS Appl. Mater. Interfaces* **2016**, *8*, 12859–12870.
[16] A. Hussain, U. Shahbaz, S. Khan, S. Basharat, K. Ahmad, F. Khan, X. Xia, *Res.* **2022**, *15*, 1854–1871.
[17] K. I. Ozoemena, *RSC Adv.* **2016**, *6*, 89523–89550.
[18] J. Melke, A. Schoekel, D. Dixon, C. Cremers, D. E. Ramaker, C. Roth, *J. Phys. Chem. C* **2010**, *114*, 5914–5925.
[19] A. S Arup Mahata, B. P. Nair, *Catalysis Science and Technology* **2019**, *9*, 4835–4863.
[20] P. Hauenstein, D. Seeberger, P. Wasserscheid, S. Thiele, *Electrochem. Commun.* **2020**, *118*, 106786.
[21] I. Mangoufis-Giasin, O. Piqué, P. Khanipour, K. J. Mayrhofer, F. Calle-Vallejo, I. Katsounaros, *J. Catal.* **2021**, *400*, 166–172.
[22] P. Khanipour, F. D. Speck, I. Mangoufis-Giasin, K. J. J. Mayrhofer, S. Cherevko, I. Katsounaros, *ACS Appl. Mater. Interfaces* **2020**, *12*, 33670–33678.
[23] M. Brodt, K. Müller, J. Kerres, I. Katsounaros, K. Mayrhofer, P. Preuster, P. Wasserscheid, S. Thiele, *Energy Tech.* **2021**, *9*, 2100164. DOI: 10.1002/ente.202100164.
[24] I. Mangoufis-Giasin, L. Fusek, T. Yang, P. Khanipour, O. Brummel, J. Libuda, K. J. J. Mayrhofer, F. Calle-Vallejo, I. Katsounaros, *ACS Catal.* **2023**, *13*, 14562–14569.
[25] A. K. Sahu, D. K. Dash, K. Mishra, S. P. Mishra, R. Yadav, P. Kashyap, in *Noble and Precious Metals - Properties, Nanoscale Effects and Applications*, ed. M. S. Seehra, A. D. Bristow, InTech, **2018** Properties and Applications of Ruthenium, 377–390.
[26] Critical Raw Materials Resilience: Charting a Path towards greater Security and Sustainability, https://eur-lex.europa.eu/legal-content/EN/TXT/PDF/?uri=CELEX:52020DC0474.accessed February 2024
[27] M. S. Chen, D. W. Goodman, *Science (New York, N.Y.)* **2004**, *306*, 252–255.
[28] L. García-Cruz, V. Montiel, J. Solla-Gullón, *Physical Sciences Reviews* **2019**, *4*, 20170124 DOI: 10.1515/psr-2017-0124.
[29] Q. Li, L. Wu, G. Wu, D. Su, H. Lv, S. Zhang, W. Zhu, A. Casimir, H. Zhu, A. Mendoza-Garcia, S. Sun, *Nano Lett.* **2015**, *15*, 2468–2473.
[30] M. S. Çögenli, A. B. Yurtcan, *Int. J. Hydrog. Energy* **2018**, *43*, 10698–10709.
[31] Y.-Z. Guo, S.-Y. Yan, C.-W. Liu, T.-F. Chou, J.-H. Wang, K.-W. Wang, *J. Mater. Chem. A* **2017**, *5*, 14355–14364.
[32] Z. Liu, G. S. Jackson, B. W. Eichhorn, *Angewandte Chemie* **2010**, *122*, 3241–3244.
[33] M. Arenz, V. Stamenković, B. Blizana, K. Mayrhofer, N. M. Marković, P. N. Ross, *J. Catal.* **2005**, *232*, 402–410.
[34] T. Shubina, M. Koper, *Electrochim. Acta* **2002**, *47*, 3621–3628.
[35] H. Huang, O. F. Blackman, V. Celorrio, A. E. Russell, *Electrochim. Acta* **2021**, *390*, 138811.
[36] X. Wang, L. Altmann, J. Stöver, V. Zielasek, M. Bäumer, K. Al-Shamery, H. Borchert, J. Parise, J. Kolny-Olesiak, *Chem. Mater.* **2013**, *25*, 1400–1407.
[37] F. Colmati, M. Magalhães, R. Sousa, E. Ciapina, E. Gonzalez, *Int. J. Hydrog. Energy* **2019**, *44*, 28812–28820.
[38] D. Godoi, J. Perez, H. M. Villullas, *J. Power Sources* **2010**, *195*, 3394–3401.
[39] R. Rizo, R. M. Arán-Ais, E. Padgett, D. A. Muller, M. J. Lázaro, J. Solla-Gullón, J. M. Feliu, E. Pastor, H. D. Abruña, *J. Am. Chem. Soc.* **2018**, *140*, 3791–3797.
[40] S.-C. L. Jee-Yee Chen, H.-Y. T. Chun-Hong Kuo, *J. Colloid Interface Sci.* **2019**, *545*, 54–62.
[41] C. Cui, L. Gan, M. Heggen, S. Rudi, P. Strasser, *Nature Mater.* **2013**, *12*, 765–771.
[42] R. Ferrando, *Frontiers in Nanoscience* **2016**, *10*, 229–243.
[43] J. T. L. Gamler, H. M. Ashberry, S. E. Skrabalak, K. M. Koczkur, *Adv. Mater.* **2018**, *30*, 1801563.
[44] V. Stamenković, M. Arenz, B. B. Blizanac, K. Mayrhofer, P. N. Ross, N. M. Marković, *Surf. Sci.* **2005**, *576*, 145–157.
[45] L. Wu, A. P. Fournier, J. J. Willis, M. Cargnello, C. J. Tassone, *Nano Lett.* **2018**, *18*, 4053–4057.
[46] M. Liu, W. Tang, Z. Xie, H. Yu, H. Yin, Y. Xu, S. Zhao, S. Zhou, *ACS Catal.* **2017**, *7*, 1583–1591.
[47] D. D. Spasov, N. A. Ivanova, A. S. Pushkarev, *Catalysts* **2019**, *9*, 803.
[48] T. Herranz, S. García, M. V. Martínez-Huerta, M. A. Peña, J. Fierro, F. Somodi, I. Borbáth, K. Majrik, A. Tompos, S. Rojas, *Int. J. Hydrog. Energy* **2012**, *37*, 7109–7118.
[49] R. Alcala, J. W. Shabaker, G. W. Huber, M. A. Sanchez-Castillo, J. A. Dumesic, *J. Phys. Chem. B* **2005**, *109*, 2074–2085.
[50] G. J. Rees, S. T. Orr, L. O. Barrett, J. M. Fisher, J. Houghton, G. H. Spikes, B. R. C. Theobald, D. Thompsett, M. E. Smith, J. V. Hanna, *PCCP* **2013**, *15*, 17195–17207.
[51] M. Wang, L. Árnadóttir, Z. J. Xu, Z. Feng, *Nano-micro letters* **2019**, *11*, 47.
[52] K. Zhao, X. Jiang, X. Wu, H. Feng, X. Wang, Y. Wan, Z. Wang, N. Yan, *Chem. Soc. Rev.* **2024**, *53*, 6917–6959. DOI: 10.1039/d3cs00840a.
[53] T. Ma, S. Wang, M. Chen, R. V. Maligal-Ganesh, L.-L. Wang, D. D. Johnson, M. J. Kramer, W. Huang, L. Zhou, *Chem.* **2019**, *5*, 1235–1247.
[54] F. Colmati, G. Tremiliosi-Filho, E. R. Gonzalez, A. Berná, E. Herrero, J. M. Feliu, *Faraday Discuss.* **2008**, *140*, 379–97; discussion 417–37.
[55] M. M. Magalhães, J. F. Gomes, G. Tremiliosi-Filho, P. B. S. de Figueiredo, R. B. de Lima, F. Colmati, *J. Appl. Electrochem.* **2021**, *51*, 173–181.
[56] Y. Weishen, L. Liwu, F. Yining, Z. Jingling, *Catal. Lett.* **1992**, *12*, 267–276.
[57] C. Kappenstein, M. Guérin, K. Lázár, K. Matusek, Z. Paál, *Faraday Trans.* **1998**, *94*, 2463–2473.
[58] J. L. Margitfalvi, I. Borbáth, K. Lázár, E. Tfirst, A. Szegedi, M. Hegedűs, S. Gőbölös, *J. Catal.* **2001**, *203*, 94–103.
[59] J. Serranoruiz, G. W. Huber, M. A. Sanchez-Castillo, J. A. Dumesic, F. Rodriguezreinoso, A. Sepulvedaescribano, *J. Catal.* **2006**, *241*, 378–388.
[60] S. Beniwal, W. Chai, K. Metavarayuth, T. D. Maddumapatabandi, D. M. Shakya, G. Henkelman, D. A. Chen, *J. Phys. Chem. C* **2021**, *125*, 17671–17683.
[61] Y. Jugnet, D. Loffreda, C. Dupont, F. Delbecq, E. Ehret, F. J. Cadete Santos Aires, B. S. Mun, F. Aksoy Akgul, Z. Liu, *J. Phys. Chem. Lett.* **2012**, *3*, 3707–3714.
[62] W. D. Michalak, J. M. Krier, S. Alayoglu, J.-Y. Shin, K. An, K. Komvopoulos, Z. Liu, G. A. Somorjai, *J. Catal.* **2014**, *312*, 17–25.
[63] H. J. Wallander, D. Gajdek, S. Albertin, G. Harlow, N. Braud, L. Buß, J.-O. Krisponeit, J. I. Flege, J. Falta, E. Lundgren, L. R. Merte, *ACS Catal.* **2023**, *13*, 16158–16167.
[64] D. Teschner, A. Wootsch, Z. Paál, *Appl. Catal, A* **2012**, *411–412*, 31–34.
[65] B.-J. Su, K.-W. Wang, C.-J. Tseng, K.-T. Lu, C.-W. Pao, J.-F. Lee, H.-S. Sheu, K.-H. Wu, J.-Y. Juang, J.-M. Chen, *ChemCatChem* **2021**, *13*, 382–387.
[66] A. Bocarsly, D. M. P. Mingos, eds, *Fuel Cells, Hydrogen Storage*, Springer Berlin Heidelberg, Berlin, Heidelberg, **2011**.
[67] J. Flórez-Montaño, G. García, J. L. Rodríguez, E. Pastor, P. Cappellari, G. A. Planes, *J. Power Sources* **2015**, *282*, 34–44.
[68] Q. Wang, G. Q. Sun, L. H. Jiang, Q. Xin, S. G. Sun, Y. X. Jiang, S. P. Chen, Z. Jusys, R. J. Behm, *PCCP* **2007**, *9*, 2686–2696.
[69] M. Roca-Ayats, O. Guillén-Villafuerte, G. García, M. Soler-Vicedo, E. Pastor, M. V. Martínez-Huerta, *Appl. Catal, B* **2018**, *237*, 382–391.
[70] Z.-Q. Zhang, Y.-C. Pei, M.-J. Xiao, G. Hu, Z.-P. Huang, T. Song, Q. Wang, W.-Y. Huang, Y. Peng, H.-L. Zhang, *Chemical communications (Cambridge, England)* **2021**, *57*, 5454–5457.
[71] R. Rizo, M. J. Lázaro, E. Pastor, G. García, *Molecules (Basel, Switzerland)* **2016**, *21*, 1225 DOI: 10.3390/molecules21091225.
[72] G. Wedler, *Lehrbuch der physikalischen Chemie*, 3rd edn, VCH, Weinheim, **1987**.
[73] Y. Zeng, X. Li, J. Wang, M. T. Sougrati, Y. Huang, T. Zhang, B. Liu, *Chem Catalysis* **2021**, *1*, 1215–1233.
[74] F. A. Stevie, C. L. Donley, *Journal of Vacuum Science & Technology A: Vacuum, Surfaces, and Films* **2020**, *38*, DOI: 10.1116/6.0000412.
[75] J. I. J. Choi, T.-S. Kim, D. Kim, S. W. Lee, J. Y. Park, *ACS Nano* **2020**, *14*, 16392–16413.
[76] M. Vandichel, A. Moscu, H. Grönbeck, *ACS Catal.* **2017**, *7*, 7431–7441.
[77] S. Sahebdelfar, M. T. Ravanchi, *Int. J. Hydrog. Energy* **2023**, *48*, 24709–24729.

[78] J. Li, S. Sharma, K. Wei, Z. Chen, D. Morris, H. Lin, C. Zeng, M. Chi, Z. Yin, M. Muzzio, M. Shen, P. Zhang, A. A. Peterson, S. Sun, *J. Am. Chem. Soc.* **2020**, *142*, 19209–19216.
[79] F. Xing, J. Ma, K.-I. Shimizu, S. Furukawa, *Nat Commun.* **2022**, *13*, 5065.
[80] W. Chen, S. Luo, M. Sun, X. Wu, Y. Zhou, Y. Liao, M. Tang, X. Fan, B. Huang, Z. Quan, *Advanced materials (Deerfield Beach, Fla.)* **2022**, *34*, e2206276.

Manuscript received: February 25, 2024
Revised manuscript received: July 30, 2024
Version of record online: October 9, 2024